The bone microenvironment invigorates metastatic seeds for further dissemination

Weijie Zhang[1,2,3], Igor L. Bado[1,2,3], Jingyuan Hu[4,5], Ying-Wooi Wan[5,6], Ling Wu[1,2,3], Hai Wang[1,2,3], Yang Gao[1,2,3], Hyun Hwan Jeong[4,6], Zhan Xu[1,2,3], Xiaoxin Hao[1,2,3], Bree M. Lege[1, 6], Rami Al-Ouran[4,7], Lucian Li[4,7], Jiasong Li[8], Liqun Yu[1,2,3], Swarnima Singh[1,2,3], Hin-Ching Lo[1,2,3], Muchun Niu[9], Jun Liu[1,2,3], Weiyu Jiang[1,2,3], Yi Li[1,2,3], Stephen T.C. Wong[8], Chonghui Cheng[1,6], Zhandong Liu[4,6], and Xiang H.-F. Zhang[1,2,3,10,11,*].

[1]Lester and Sue Smith Breast Center, Baylor College of Medicine, One Baylor Plaza, Houston, TX 77030, USA

[2]Dan L. Duncan Cancer Center, Baylor College of Medicine, One Baylor Plaza, Houston, TX 77030, USA

[3]Department of Molecular and Cellular Biology, Baylor College of Medicine, One Baylor Plaza, Houston, TX 77030, USA

[4]Jan and Dan Duncan Neurological Research Institute, Texas Children's Hospital, Houston, TX 77030, USA

[5]Quantitative and Computational Biosciences Program, Baylor College of Medicine, One Baylor Plaza, Houston, TX 77030, USA

[6]Department of Molecular and Human Genetics, Baylor College of Medicine, Houston, Texas 77030, USA

[7]Department of Pediatrics, Baylor College of Medicine, Houston, Texas 77030, USA

[8]Department of Systems Medicine and Bioengineering, Houston Methodist Research Institute, Houston, TX 77030, USA

[9]Integrative Molecular and Biomedical Sciences Graduate Program, Baylor College of Medicine, One Baylor Plaza, Houston, TX 77030, USA

[10]McNair Medical Institute, Baylor College of Medicine, BCM600, One Baylor Plaza, Houston, TX 77030, USA

[11]Lead Contact

*Correspondence: xiangz@bcm.edu

SUMMARY

Metastasis has been considered as the terminal step of tumor progression. However, recent genomic studies suggest that many metastases are initiated by further spread of other metastases. However, the corresponding pre-clinical models are lacking and the underlying mechanisms are elusive. Using several approaches including parabiosis and an evolving barcode system, we demonstrated that the bone microenvironment facilitates breast and prostate cancer cells to further metastasize and establish multi-organ secondary metastases. We uncovered that this metastasis-promoting effect is driven by epigenetic reprogramming that confers stem-like properties on cancer cells disseminated from bone lesions. Consistent with the accompanied study, we discovered that enhanced EZH2 activity mediates the increased stemness and metastasis capacity. The same findings also apply to single cell-derived populations, indicating mechanisms distinct from clonal selection. Taken together, our work revealed an unappreciated role of the bone microenvironment in metastasis evolution, and elucidated an epigenomic reprogramming process driving terminal-stage, multi-organ metastasis.

INTRODUCTION

Metastasis to distant organs is the major cause of cancer-related deaths. Bone is the most frequent destination of metastasis in breast cancer and prostate cancer (Gundem et al., 2015; Kennecke et al., 2010; Smid et al., 2008). In the advanced stage, bone metastasis is driven by the paracrine crosstalk among cancer cells, osteoblasts, and osteoclasts, which together constitute an osteolytic vicious cycle (Esposito et al., 2018; Kang et al., 2003; Kingsley et al., 2007; Weilbaecher et al., 2011). Specifically, cancer cells secrete molecules such as PTHrP, which act on osteoblasts to modulate the expression of genes including RANKL and OPG (Boyce et al., 1999; Juárez and Guise, 2011). The alterations of these factors in turn boost osteoclast maturation and accelerate bone resorption. Many growth factors (e.g., IGF1) deposited in the bone matrix are then released, and reciprocally stimulate tumor growth. This knowledge laid the foundation for clinical management of bone metastases (Coleman et al., 2008).

The urgency of bone metastasis research is somewhat controversial. It has long been noticed that, at the terminal stage, breast cancer patients usually die of metastases in multiple organs. In fact, compared to metastases in other organs, bone metastases are relatively easier to manage. Patients with the skeleton as the only site of metastasis usually have better prognosis than those with visceral organs affected (Coleman and Rubens, 1987; Coleman et al., 1998). These facts argue that perhaps metastases in more vital organs should be prioritized in research. However, metastases usually do not occur synchronously. In 45% of metastatic breast cancer cases, bone is the first organ that shows signs of metastasis, much more frequently compared to the lungs (19%), liver (5%) and brain (2%) (Coleman and Rubens, 1987). More importantly, in more than two-thirds of cases, metastases will not be limited to the skeleton, but rather subsequently occur to other organs and eventually cause death (Coleman, 2006; Coleman and Rubens, 1987; Coleman et al., 1998). This raises the possibility of secondary dissemination from the initial bone lesions to other sites. Indeed, recent genomic analyses concluded that the majority of metastases result from seeding from other metastases, rather than primary tumors (Brown et al., 2017; Gundem et al., 2015; Ullah et al., 2018). Thus, it is imperative to investigate further metastatic seeding from bone lesions, as it might lead to prevention of the terminal stage, multi-organ metastases that ultimately cause the vast majority of deaths.

Despite its potential clinical relevance, little is known about metastasis-to-metastasis seeding. Current preclinical models focus on seeding from primary tumors, but cannot distinguish

between additional sites of dissemination. We have recently developed an approach, termed intra-iliac artery injection (IIA), that selectively deliver cancer cells to hind limb bones via the external iliac artery (Wang et al., 2015a, 2018; Yu et al., 2016). Although it skips the early steps of the metastasis cascade, it focuses the initial seeding of tumor cells in the hind limbs, and allows the tracking of secondary metastases from bone to other organs. It is, therefore, a suitable model to investigate the clinical and biological roles played by bone lesions in multi-organ metastasis-to-metastasis seeding.

RESULTS

Temporally lagged multi-organ metastases in mice carrying IIA-introduced bone lesions of breast and prostate cancers.

IIA injection has been employed to investigate early-stage bone colonization. Both aggressive (e.g., MDA-MB-231) and relatively indolent (e.g. MCF-7) breast cancer cells can colonize bones albeit following different kinetics. In both cases, cancer cell distribution is highly bone-specific at early time points, allowing us to dissect cancer-bone interactions without the confounding effects of tumor burden in other organs (Figure 1A) (Wang et al., 2015a, 2018). However, as bone lesions progress, metastases, as indicated by bioluminescence signals, begin to appear in other organs, including additional bones, lungs, liver, kidney, and brain, usually 4-8 weeks after IIA injection of MDA-MB-231 cells (Figure 1B). Bioluminescence provides sensitive detection of metastasis (Deroose et al., 2007). However, many factors such as lesion depth and optical properties of tissues may influence signal penetration. Thus, we used a number of other approaches to validate the presence of metastases in multiple tissues. These include positron emission tomography (PET) (Figure 1C), micro computed tomography (μCT) (Figure 1C and S1A), whole-tissue two-photon imaging (Figure S1B), immunofluorescence staining (Figure 1D and 1E), and histological staining (H&E) (Figure S1C). Compared to bioluminescence imaging, these approaches provided independent evidence, but are either less sensitive or non-quantitative (Deroose et al., 2007) (Figure S1A). Therefore, we also used quantitative PCR (qPCR) to detect human-specific DNA in dissected mouse tissues, and confirmed that qPCR results and bioluminescence signal intensity values are highly correlative (Figure S1D and S1E). Of note, the spectrum of metastases covers multiple bones (Figure 1D) and soft-tissue organs (Figure 1E). Taken together, our data support the occurrence of multi-organ metastases in animals with IIA-introduced bone lesions.

This phenomenon is not specific for the highly invasive MDA-MB-231 cells, but was also observed in more indolent MCF-7 cells and PC3 prostate cancer cells, as well as murine

mammary carcinoma AT-3 cells in immune competent mice, albeit after a longer lag period for PC3 cells (8-12 weeks) (Figure 1F-1H, and S1F).

As an independent approach to introduce bone lesions, we used intra-femoral (IF) injection that delivers cancer cells directly to bone marrow, bypassing the artery circulation involved in IIA injection. This approach also resulted in multi-organ metastases at late time points in both MDA-MB-231 and AT-3 models (Figure 1I and S1G). The distribution and frequencies of metastases were similar between intra-femoral and IIA injection models (Figure 1J and 1K). Thus, we hypothesize cancer cells in the bone microenvironment may gain capacity to further metastasize.

Bone lesions more readily give rise to multi-organ metastasis

The later-appearing multi-organ metastases may result from further dissemination of cancer cells in the initial bone lesions. Alternatively, they could also arise from cancer cells that leaked and escaped from bone capillaries during IIA or IF injection. In the latter case, the leaked cancer cells would enter the iliac vein and subsequently arrive in the lung capillaries. Indeed, there did appear to be bioluminescence signals in lungs upon IIA injection (Figure 1A). To distinguish between cell leakage and dissemination, we performed intra-iliac vein (IIV) injection, and compared the results to those of IIA injection at late time points. The IIV injection procedure should mimic the “leakage” from IIA injection, although allowing many more cells to enter the venous system and be arrested in the lung capillaries (Figure 2A, S2A, S2B and S2C, compared to Figure 1A). As another relevant comparison, we also examined metastasis from orthotopic tumors transplanted into mammary fat pad (MFP) (Figure 2B, S2A, S2B and S2D). Furthermore, in the case of ER+ cells, recent studies suggest that intra-ductal injection provides a more “luminal” microenvironment and may promote spontaneous metastasis to other organs (Sflomos et al., 2016). Therefore, we also included the mouse mammary intra-ductal (MIND) method as an additional approach to test MCF-7 cells, the only ER+ cancer model in our study. In all experiments, we used total bioluminescence signal intensity to evaluate tumor burdens at hind limbs (IIA and IF), lungs (IIV) and mammary fat pads (MFP and MIND), respectively. We attempted to assess multi-organ metastasis when the “primary lesions” reach comparable level, simply to rule out the size of the original tumors as a confounding factor in our comparisons. This was feasible for some models such as mammary tumors and bone lesions derived from MCF-7 (Figure S2E). However, in other models, mammary tumors tend to grow much faster compared to lesions growing in other sites (Figure S2F and S2G). Therefore, we chose to end experiments at the same time point for all conditions. In all experiments, multi-organ metastases

were examined well before animals became moribund. Taken together, we set to ask if secondary metastasis from bone lesions follows a faster kinetics and reaches a wider spectrum of target organs as compared to that from orthotopic tumors or lungs.

Strikingly, the answer to this question is evidently positive in all three tumor models examined (Figure 2C-2H). We assessed 11 organs including six other bones and five soft tissue organs for metastasis. Curiously, in many cases, counter-lateral hind limbs (designated as "L.Hindlimb" for "left hind limb" as the initial bone lesions were introduced to the right hind limb) are most frequently affected among all organs in IIA models. Lungs are also frequently affected in MDA-MB-231 and AT-3 models, by metastasis from both bone lesions and orthotopic tumors. However, it is striking to note that lung metastasis in IIA and IF models is comparable or even more severe as compared to that in IIV models, despite the fact that IIV injection delivers more cancer cells directly to lungs (Figure S2H). In fact, the normalized increase of tumor burden at lungs through IIA and IF, are at least 10 fold more than that through IIV injection (e.g., Figure S2H), which strongly argue that bone microenvironment promotes secondary metastasis.

Cross-seeding of cancer cells from bone lesions to orthotopic tumors.

Cancer cells may enter circulation and seed other tumor lesions or re-seed the original tumors (Kim et al., 2009). By using MDA-MB-231 cells tagged with different fluorescent proteins, we asked if bone lesions can cross-seed mammary tumors (Figure 3A). Interestingly, we observed that while orthotopic tumors can be readily seeded by cells derived from bone lesions, the reverse seeding rarely occurs (Figure 3B and 3C). This difference further highlights the enhanced metastatic aggressiveness of cancer cells in the bone microenvironment.

Parabiosis models support enhanced capacity of cancer cells to metastasize from bone to other organs.

It is possible that IIA injection disturbs bone marrow and stimulates systemic effects that allow multi-organ metastases. For example, the injection might cause a transient efflux of bone marrow cells that can arrive at the distant organ to form a pre-metastatic niche. To test this possibility, we used parabiosis to fuse the blood circulation between a bone lesion-carrying mouse (donor) and tumor-free mouse (recipient) one week after IIA injection. In parallel, we also performed parabiosis on donors that have received MFP injection and tumor-free recipients (Figure 3D). After seven weeks, surgical separation was performed to allow time for metastasis development in the recipient mice. Subsequently, the organs of originally tumor-free recipients were collected and examined for metastases four months later. Only ~20% of recipients in the

IIA group were found to harbor cancer cells in various organs (Figure 3E and 3F), mostly as microscopic disseminated tumor cells (Figure 3G), indicating that the fusion of circulation system is not efficient for metastatic seeds to cross over from donor to recipient. However, in the MFP comparison group, no metastatic cells were detected (Figure 3F, S3A, and S3B), and the difference is statistically significant. Therefore, the parabiosis data also support the hypothesis that the bone microenvironment invigorates further metastasis, and this effect is unlikely to be due to IIA injection-related systemic influence.

An evolving barcode system revealed the phylogenetic relationships between initial bone lesions and secondary metastases.

Barcoding has become widely used to elucidate clonal evolution in tumor progression and therapies. An evolving barcoding system has recently been invented for multiple parallel lineage tracing (Kalhor et al., 2017, 2018). It is based on CRISPR/Cas9 system, but utilizes guide RNAs that are adjacent to specific protospacer adjacent motif (PAM) in their genomic locus, thereby allowing Cas9 to mutate its own guide RNAs. These variant guide RNAs are named homing guide RNAs (hgRNAs). When Cas9 is inducibly expressed, hgRNA sequences randomly drift, serving as evolving barcodes (Figure 4A). A preliminary in vitro experiment demonstrated that the diversity of barcodes (measured as Shannon entropy) is a function of duration of Cas9 expression (Figure 4B, and S4A).

We introduced this system into MDA-MB-231 and AT-3 cells, and transplanted them into mammary fat pads of nude and wild-type C57BL/6 mice, respectively. When orthotopic tumors reach 1 cm^3, we resected the tumors and induced Cas9 by doxycycline. It should be noted that the orthotopic tumors already harbored a high diversity of mutant barcodes presumably due to leakage of Cas9 expression. This served as an initial barcode repertoire that enabled us to distinguish distinct clones that metastasize from orthotopic tumors to various organs. Further Cas9 expression yielded new mutations for delineation of parent-child relationship among lesions (Figure 4C). We rationalize that the diversity of barcodes, or the Shannon entropy, in a metastasis should reflect the “age” of metastasis. When secondary metastasis occurs, child metastases will inherit only a subset of barcodes causing a reduction of Shannon entropy. Therefore, among genetically related metastases indicated by sharing common mutant barcodes, those with higher Shannon entropy are more likely to be parental (Figure 4C). This can be supported by the observation that primary bone lesions possess higher entropy than those secondary metastases in IIA model (Figure S4B).

We isolated 32, 29, 9 and 17 metastases from two mice bearing MDA-MB-231 and two mice bearing AT3 tumors, respectively (Figure 4D, S4C and Supplementary Table 1). Sequencing of the barcodes carried by these metastases in combination of the analysis of the timing of seeding as indicated by the Shannon entropy of barcodes led to profound findings. First, at the terminal stage, multi-organ metastases are not genetically grouped according to sites of metastases (Fig. 4E and S4D). Nonnegative Matrix Factorization (NMF) analysis of mutant barcodes suggested the early disseminated metastases, which have highest level of Shannon entropy, were featured with a common cluster of mutant barcodes irrespective of their locations, especially in AT-3 models (Fig. 4F, S4E and S4F). This is evidence against organotropism in the late stage of metastatic progression in mouse models. Second, most metastases are potentially multiclonal as indicated by multiple clusters of independent mutant barcodes (Figure. 4F and S4F). Third, putative parent-child relationship between metastases with unique mutant barcodes clearly exemplified secondary metastatic seeding from bone to other distant sites (Figure 4G and S4G) in both models. Finally, we did not observe a clear correlation between tumor burden and Shannon entropy across different metastases, and the putative founder metastases can be small in tumor burden while diversified in barcode composition, suggesting that asymptomatic metastases might also seed further metastases (Figure S4H and S4I). Taken together, these data reveal potential wide-spread metastasis-to-metastasis seedings, and support that secondary metastasis from bone to other distant organs happens in a natural metastasis cascade.

The bone microenvironment promotes further metastasis by enhancing cancer cell stemness and plasticity

Organo-tropism is an important feature of metastasis. Clonal selection appears to play an important role in organ-specific metastasis, which has been intensively studied previously (Bos et al., 2009; Kang et al., 2003; Minn et al., 2005; Vanharanta and Massague, 2013). Herein, the metastasis-promoting effects of the bone microenvironment appear to be multi-organ and do not show specific organ-tropism. In an accompanied study, we discovered profound phenotypic shift of ER+ breast cancer cells in the bone microenvironment, which included loss of luminal features and gain of stem cell-like properties (Bado et al., 2019). This shift is expected to promote further metastases (Gupta et al., 2019; Ye and Weinberg, 2015). Therefore, we hypothesize that the enhancement of metastasis may be partly through an epigenomic dedifferentiation process.

To test this possibility, we compared the metastasis capacity of a genetically identical SCP of MDA-MB-231 cells and its derivatives entrained by different microenvironments (Figure S5A). Based on a previous study (Minn et al., 2005) , we picked a non-metastatic SCP termed SCP21. SCP21 cells were introduced to mammary fat pads, lungs, and hind limb bones to establish tumors. After 6 weeks, entrained cancer cells were extracted from these organs for further experiments (Figure 5A). We used intra-cardiac injection to simultaneously deliver cancer cells to multiple organs (Figure 5A). Compared to the mammary fat pad- and lung-entrained counterparts, bone-entrained SCP21 was more capable of colonizing distant organs and gave rise to much higher tumor burden in multiple sites as determined by bioluminescence (Figure 5A-5C). In mice subjected to dissection and *ex vivo* bioluminescent imaging, significantly more and bigger lesions were observed from mice that received bone-entrained SCP21 cells in both skeletal and visceral tissues (Figure S5B-5D), suggesting an increase of overall metastatic capacity rather than bone tropism in tumor cells exposed to bone environment.

Inspired by the accompanied study (Bado et al., 2019) , we examined stem cell markers of SCP21 cells entrained in different microenvironment. Interestingly, bone-entrained cells appeared to express a higher level of both ALDH1 activity and CD44 expression (Figure 5D and 5E). In addition, bone-entrained SCP21 cells increased expression of multiple proteins involved in epithelial-mesenchymal transition (EMT) and in pathways shown to mediate the effects of bone microenvironment on ER+ cancer cells in our accompanied study, including FGFR1, PDGFRβ, EZH2, SLUG and ZEB1 (Figure 5F and S5E). These data suggest that similar mechanisms may be at work to induce cancer cell stemness and plasticity in this ER- model.

Indeed, when the same approaches were applied to the SCP2 derivatives of MCF-7 cells. Bone entrained SCP2 cells showed increased initial survival and faster metastatic growth after intra-cardiac injection (Figure 5G-5I), and increased level of ALDH1 activity and CD44 expression (Figure 5J and 5K). In this more epithelial model, we also observed a hybrid EMT phenotype (Figure S5F), as also elaborated in our associated studies. It should be noted that, in this series of experiments, lung-derived subline was not developed due to the lack of lung colonization for SCP2 cells.

In addition to cancer cells that are manually extracted from various organs, we also examined naturally occurred circulating tumor cells (CTCs) emitted from bone lesions versus mammary tumors. Not surprisingly, bone lesions generated a higher number of CTCs, probably due to the more permeable vascular structures or the survival advantages conferred by bone. However, on

top of their higher number, CTCs from bone lesions also express higher levels of CD44 and ALDH1 (Figure 5L and 5M), suggesting increased stemness.

Finally, we also interrogated CD44 expression in a single-cell RNA-seq dataset derived from breast cancer patients. When patients were divided into two groups – those carrying bone metastasis versus those carrying other metastases, significantly higher expression of CD44 was observed in the former (Figure 5N) (Aceto et al., 2018), providing clinical support for our hypothesis that the bone microenvironment promotes tumor cell stemness and plasticity, and thereby invigorate further metastasis.

EZH2 in cancer cells orchestrates the effect of bone microenvironment in secondary metastasis

Since EZH2 was revealed to play a central role in loss of ER and gain of plasticity in ER+ models in the accompanied study (Bado et al., 2019), we asked if it also mediates secondary metastasis. We used an EZH2 target gene signature (Lu et al., 2010) to deduce EZH2 enzymatic activities, and performed RNA-seq transcriptomic profiling of SCP21 cells subjected to various treatments or entrained in different organs. The validity of the EZH2 signature was first tested by treatment of EPZ011989 (EPZ), an inhibitor of EZH2 methyltransferase activity. EPZ relieved the suppression of signature genes, resulting in their higher expression (Figure S6A). The frequency of ALDH1+ cells and the expression of mesenchymal and stemness markers in bone-entrained SCP21 cells were also significantly decreased upon EPZ treatment (Figure S6B-D). We then compared cell entrained in bone lesions versus mammary gland tumors or lung metastasis and discovered higher EZH2 activity in the bone (Figure 6A). Importantly, bone-induced changes to both EZH2 activity and frequency of ALDH1+ cells appeared to be reversible, as *in vitro* passages progressively led to loss of these traits (Figure 6B and 6C). Other bone microenvironment-induced factors upstream of EZH2 (e.g., FGFR1 and PDGFRβ) (Kottakis et al., 2011; Yue et al., 2019) exhibited transient increased expression in bone-entrained cells (Figure 6D and S6E).

Remarkably, transient treatment of EPZ before intra-cardiac injection, which did not suppress the growth of tumor cells *in vitro* (Figure S6F), completely abolished the enhanced metastasis of bone-entrained SCP21 cells (Figure 6E-6G) and SCP2 cells (Figure 6H-6K) *in vivo*, again suggesting that the observed effects of bone microenvironment is not through clonal selection, but rather epigenomic reprogramming.

Finally, to confirm the intrinsic role of EZH2 in cancer cells during this process, we generated inducible knockdown of EZH2 (Figure S6G), which also slightly affected downstream expression of plasticity factors and stem cell markers (Figure S6G-H) but did not alter cancer cell growth rate *in vitro* (Figure S6I). Induction of knockdown was initiated after bone lesions were introduced for one week (Figure 6L, and S6J). Interestingly, whereas EZH2 knockdown did not alter primary bone lesion development (Figure 6M), it dramatically reduced secondary metastasis to other organs (Figure 6N). Taken together, these above results strongly implicate EZH2 as a master regulator of secondary metastases from bone lesions.

DISCUSSION

In this study, based on the IIA injection technique and through multiple independent approaches, we demonstrated that the bone microenvironment not only permits cancer cells to further disseminate but also appears to augment this process. A key question that remains is the timing of secondary metastasis spread out of the initial bone lesions: whether this occurs before or after the bone lesions become symptomatic and clinically detectable. The answer will determine if therapeutic interventions should be implemented in adjuvant or metastatic settings, respectively. Moreover, if further seeding occurs before bone lesions become overt, it raises the possibility that metastases in other organs might arise from asymptomatic bone metastases, which might warrant further investigations. Indeed, our co-submitted study indicated that in the early phase of bone colonization, cancer cells already acquire stem cell-like features (Bado et al., 2019), supporting that asymptomatic bone micrometastases are potentially capable of metastasizing before being diagnosed. In this study, our evolving barcode strategy exemplified potential metastases from bone to other organs. Interestingly, we found that the putative parental metastases could remain small (Figure S5G and S5H), which may suggest that further dissemination might occur before diagnosis of existing lesions. Future studies will be needed to precisely determine the onset of secondary metastasis from bones.

The evolving barcode strategy was useful in tracing metastatic evolution. The most striking and robust finding from these experiments is that genetically closely-related metastases do not localize in the same type of tissues and are usually highly distinct from orthotopic tumors. This in principle argues against independent seeding events from primary tumors and supports metastasis-to-metastasis seeding. However, the deduction of specific parental-child relationship based on Shannon entropy is intuitive and qualitative and needs to be formulated with more quantitative models in future work. We provided examples of bone metastases that likely seed

metastases in other organs. The prevalence of this phenomenon remains to be assessed using more sophisticated models.

The fact that the genetically homogenous SCP cells became more metastatic after lodging into the bone microenvironment suggest a mechanism distinct from genetic selection. Remarkably, this phenotype persists even after in vitro expansion, so it is relative stable and suggests an epigenomic reprogramming process, which has been characterized in depth in the accompanied study (Bado et al., 2019). We propose that this epigenetic mechanism may act in concerted with the genetic selection process. Specifically, the organ-specific metastatic traits may pre-exist in cancer cell populations (Minn et al., 2005; Zhang et al., 2013), and determine the first site of metastatic seeding. The epigenomic alterations will then occur once interactions with specific microenvironment niches are established and when cancer cells become exposed chronically to the foreign milieu of distant organs. Our data suggest that such alterations drive a second wave of metastases in a less organ-specific manner (Figure 6O). This may explain why terminal stage of breast cancer is often associated with multiple metastases (DiSibio and French, 2008).

Here we suggested that the enhanced EZH2 activity underpins the epigenetic reprograming of tumor cells in bone microenvironment for further metastases. EZH2 maintains the de-differentiated and stem-like status of breast cancer cells by repressing the lineage-specific transcriptional programs (Chang et al., 2011; Gonzalez et al., 2014). Pharmacologically or genetically targeting EZH2 has been reported to inhibit breast cancer growth and metastases with different efficacies in preclinical models (Hirukawa et al., 2018; Ma et al., 2020; Zhang et al., 2020). It was noted that in our models, EZH2 inhibition could not suppress the cell growth *in vitro* or in the primary injection site, whereas both the transient treatment of EZH2 inhibitor or inducible knock-down of EZH2 in cancer cells dramatically decreased the metastases, suggesting targeting EZH2 may block the metastatic spread rather than the growth of tumor. However, due to the broad effects on transcription and unspecific targeting, caution must be taken for the therapeutic design of EZH2 inhibitors. In line with such notions, systemic administration of EZH2 inhibitor showed minimal effect in decreasing secondary metastases from established bone lesions in our models (data not shown), which was likely due to the profound effects of EZH2 inhibition on the microenvironments or the lack of inhibition on the catalytic-independent functions of EZH2 protein (Anwar et al., 2018; Qiao et al., 2016; Zhang et al., 2020; Zhao et al., 2016).

In the clinic, some bone metastases can be managed for years without further progression, while others quickly develop therapeutic resistance and are associated with subsequent

metastases in other organs (Coleman, 2006). These different behaviors may suggest different subtypes of cancers that are yet to be characterized and distinguished. Alternatively, there may be a transition between these phenotypes. In fact, depending on different interaction partners, the same cancer cells may exist in different status in the bone. For instance, while endothelial cells may keep cancer cells in dormancy (Ghajar et al., 2013; Price et al., 2016), osteogenic cells promote their proliferation and progression toward micrometastases (Wang et al., 2015a, 2018). Therefore, it is possible that the transition from indolent to aggressive behaviors is underpinned by an alteration of specific microenvironment niches. Detailed analyses of such alteration may be achieved will lead to unprecedented insights into metastatic progression.

Although data presented in this and accompanied studies indicate that cancer cells colonizing the bone acquire intrinsic traits for further dissemination, we cannot rule out systemic effects that may also contribute to this process. At the late stage, bone metastases are known to cause strong systemic abnormality such as cachexia (Waning et al., 2015), which may influence secondary metastasis. Even at early stages before bone metastases stimulate severe symptoms, the disturbance of micrometastases to hematopoietic cell niches may mobilize certain blood cells to migrate to distant organs, which may in turn result in altered metastatic behaviors (Peinado et al., 2017). These possibilities will need to be tested in future research.

ACKNOWLEDGEMENTS

We would like to thank Zhang Laboratory members, Dr. Lin Tian and Dr. Reza Kalhor for helpful discussion. X.H.-F.Z. is supported by US Department of Defense DAMD W81XWH-16-1-0073 (Era of Hope Scholarship), NCI CA183878, Breast Cancer Research Foundation, and McNair Medical Institute. H.W. is supported in part by US Department of Defense DAMD W81XWH-13-1-0296. This project was supported by the RNA In Situ Hybridization Core with funding from the NIH (1S10OD016167), the Cytometry and Cell Sorting Core with funding from the CPRIT Core Facility Support Award (CPRIT-RP180672), the NIH (P30 CA125123 and S10 RR024574) and the expert assistance of Dr. Cecilia Ljungberg and Joel M. Sederstrom at Baylor College of Medicine. We also acknowledge the technical assistance of the Pathology Core of Lester and Sue Smith Breast Center, the Genomic and RNA profiling core, Small Animal Imaging Facility (SAIF) core at Baylor College of Medicine and the Dan L. Duncan Cancer Center.

AUTHOR CONTRIBUTIONS

Conceptualization and Validation, W.Z., I.B., J.H., H.W., Z.L., X.H.-F.Z.; Methodology, Formal Analysis and Investigation, W.Z., I.B., J.H., Y.W., L.W., H.W., Y.G., Z.X., X.H., B.M.L, R.A., L.L., J.L., L.Y., S.S., H.L., M.N., J.L., W.J., Z.L., X.H.-F.Z.; Resources, Y.L., S.T.W., C.C., Z.L., X.H.-F.Z.; Software, Data Curation and Visualization, W.Z., I.B., J.H., Y.W., H.H.J, R.A. L.L, S.S., Z.L., X.H.-F.Z.; Writing – Original Draft, W.Z., I.B., J.H., X.H.-F.Z.; Writing – Review & Editing, W.Z., H.L., X.H.-F.Z.; Supervision, X.H.-F.Z.; Project Administration, W.Z., X.H.-F.Z.; Funding Acquisition, H.W., Z.L., X. H.-F. Z.

DECLARATION OF INTERESTS

The authors declare no competing interests.

FIGURE LEGENDS

Figure 1. Multi-organ metastases in mice carrying bone lesions.

(A) Diagram of intra-iliac artery (IIA) injection and representative bioluminescent images (BLI) showing the *in vivo* distribution of triple negative human breast cancer cells MDA-MB-231 fLuc-mRFP (MDA-MB-231 FR) cells after IIA injection. 1E5 MDA-MB-231 FR were injected via the iliac artery to the right hindlimb of 6-week old female nude mice. The animals were monitored weekly by *in vivo* BLI imaging.

(B-C) Representative *ex vivo* bioluminescent images (**B**), and PET-μCT (**C**) on hindlimbs and other tissues of the same animal with MDA-MB-231 FR cells inoculated in bone after 8 weeks. Tissues were dissected and imaged immediately after *in vivo* BLI imaging in 15 minutes. R.H, Right Hindlimb; Lu, Lung; L.H, Left Hindlimb; Li, Liver; Ki, Kidney; Sp, Spleen; Br, Brain; Ve, Vertebrae; F.L, Forelimbs; Ri, Ribs; St, Sternum; Cr, Cranium.

(D-E) Representative immunofluorescent images of RFP positive tumor lesions on skeletal tissues (**D**) and other organs (**E**). Red, tumor cells; Green, CD31/CD144+ vessels; Blue, Nucleus. Scale bar, 20 μm.

(F-H) Representative BLI images of *ex vivo* tissues and animals received 2E5 prostate cancer cells PC3 **(F)**, 1E5 estrogen receptor positive luminal breast cancer cells MCF-7 **(G)**, and 1E5 murine mammary carcinoma cells AT-3 **(H)** after the indicated period.

(I) Diagram of intra-femoral injection (IF) (Left) and representative *ex vivo* BLI images of tissues from animals received MDA-MB-231 cells (Middle) or AT-3 cells (Right) through IF injection. 1E5 MDA-MB-231 FR or AT-3 FR cells were injected directly into the right femur bone marrow cavity of 6-week old female nude or C57BL/6 mice, respectively.

(J-K) Heat map of *ex vivo* bioluminescent intensity and status of metastatic involvement at tissues of animals carried MDA-MB-231 (**J**) and AT-3 (**K**) bone tumors through IIA or IF injection. Each column represents an individual animal, and each row represents a type of tissues or status of multi-site metastases. Gray cells indicate the tissues without detectable lesions. Hereafter, the presence of metastatic lesions is defined as the detection of clustered, normally distributed BLI signals above 15 counts/pixel under 120 seconds exposure time. The status of 'multi-site metastases' is defined as the metastatic involvement of at least 3 tissues other than the primary implantation site (IIA or IF, right hindlimb; IIV, lung; MFP or MIND, mammary gland). The metastatic burden refers to the total BLI intensity per second in a defined region of interest for each type of tissues

(count/s). N (# of mice) = 16 (IIA MDA-MB-231); 11 (IF MDA-MB-231); 10 (IIA AT-3); 10 (IF AT-3). *P* values were determined by Fisher's exact test on the frequency of metastatic involvement while by Mann-Whitney test of on the metastatic burden. See also Figure S1.

Figure 2. The specificity of bone microenvironment in promoting further metastasis

(A) Diagram of intra-iliac vein (IIV) injection, and representative BLI images of animals and tissues 8 weeks after receiving 1E5 IIV injected MDA-MB-231 FR cells.

(B) Diagram of mammary fat pad implantation (MFP), and representative BLI images of animals and tissues 8 weeks after receiving 1E5 MDA-MB-231 FR cells in mammary fat pads.

(C-D) Comparison of frequencies of metastatic involvement and the metastatic burden at each tissue (**C**) and the ratio of multi-site metastases (**D**) in animals carrying bone metastases (IIA and IF model), lung metastases (IIV model) or mammary tumors (MFP model) after 8-week inoculation of same number of MDA-MB-231 cells. N (# of mice) = 27 (Bone); 18 (Mammary Tumor); 10 (Lung).

(E-F) Comparison of frequencies of metastatic involvement and the metastatic burden at each tissue (**E**) and the ratio of multi-site metastases (**F**) in animals carrying bone metastases (IIA and IF model), lung metastases (IIV model) or mammary tumors (MFP model) after 23-day inoculation of same number of AT-3 cells. N (# of mice) = 20 (Bone); 11 (Mammary Tumor); 9 (Lung).

(G-H) Comparison of frequencies of metastatic involvement and the metastatic burden at each tissue (**G**) and the ratio of multi-site metastases (**H**) in animals carrying bone metastases (IIA model), lung metastases (IIV model) or mammary tumors (MFP or MIND model) after 8-week inoculation of same number of MCF-7 cells. N (# of mice) = 8 (Bone); 10 (MFP); 13 (MIND); 9 (Lung).

P values were determined by Chi-square test in **C-H** on the ratio of metastatic involvement and multi-site metastases; by uncorrected Dunn's test post Kruskal-Wallis test in **C**, **E** and **H** on the metastatic burden. See also Figure S2.

Figure 3. Cross-seeding and parabiosis experiments support the promoting effects of bone microenvironment in further metastases

(A) Schematics showing the experimental design of cross-seeding experiment between primary tumors and bone lesions. Upper, 1E5 mRFP-tagged MDA-MB-231 cells were injected via IIA to right hindlimbs and same number of EGFP-tagged MDA-MB-231 cells were implanted in the left mammary fat pads in the same animal; lower, the fluorescent protein tagged cells were swapped between bone lesions and mammary tumors.

(B) Representative confocal images showing the cross-seeding between bone metastases and mammary tumors. Red, mRFP; Green, EGFP; White, vessels; Blue, nucleus. Scale bar, 100 μm. N (# of mice) = 5 for each arm.

(C) Incidence of cross-seeding between bone lesions and mammary tumors in both directions.

(D) Schematics showing the experimental design to compare the dissemination capacity of bone metastases and primary tumors using parabiosis model. Nude mice (Donor) were implanted with 1E5 MDA-MB-231 cells via IIA (upper) or MFP (lower) injection 1 week prior to the parabiosis surgery. The donor mice and tumor-free recipient mice were surgically connected to allow the sharing of circulation. The parabiotic pairs were then maintained for 7 weeks to allow the dissemination of tumor cells from donor mice to recipient mice, before the surgical separation surgery was performed. The recipient mice were then continuously monitored with bioluminescent imaging bi-weekly till the detection of metastatic lesions or up-to 4 months. N (# of mice) = 17 (Bone); 19 (Mammary Tumor).

(E) Representative bioluminescent images showing that the metastatic lesions in recipient mice parabiotic with mice bearing bone metastases. 17 animals in total were examined.

(F) Comparison of the ratio of recipient mice showing signs of metastases as detected by BLI imaging, between bone metastases and mammary tumor (MFP) groups.

(G) Representative immunofluorescent images of tissues from recipient animals of BM group. Scale bar, 20 μm. Tissues from 6 animals were examined.

P value was determined by Fisher's exact test in **C** and **F**. See also Figure S3.

Figure 4. Metastatic evolution delineated by an evolving barcode system

(A) A schematic diagram showing the principle of the evolving barcode system comprised of homing guide RNAs (hgRNAs) and inducible Crispr-Cas9. A PAM sequence (GGG) was inserted in-between the spacer and scaffold sequence of hgRNA, which allows the self-

targeting upon the induction of Cas9 expression by Doxycycline. Random mutations can therefore be introduced on the hgRNA sequence (Kalhor et al., 2017, 2018).

(B) Dot plot showing the change of the ratio of unmutated barcode (Left Y axis) and the Shannon entropy (Right Y axis) in barcoded MDA-MB-231 cells upon multiple rounds of doxycycline treatment *in vitro*. Cells were treated with 100μg/ml doxycycline for 2 hours and then rinsed by pre-warmed PBS twice to completely remove doxycycline and then allow to grow *in vitro* for 4 days. 1 million cells were collected for barcode sequencing and 0.5 million cells were seeded back to the petri dish and received another round of doxycycline treatment 24 hours later.

(C) A schematic diagram showing the rationale of using evolving barcodes to infer the evolution history of metastatic lesions and the timing of metastatic seeding. The diversity of barcodes decreases sharply when new metastases are seeded by a few single-cells or multiple-cell clusters. Part of the parental barcodes is inherited by the children metastases. Upon Cas9 activation, barcodes in new lesions start evolving and regain diversity depending on the duration of doxycycline induction. The diversity can therefore infer the relative timing of seeding, and the related metastases share common barcodes.

(D) A schematic diagram (upper) showing the design of *in vivo* experiment using the evolving barcoding system to study the metastatic spreads and representative BLI images (lower) of metastatic lesions from mouse #510. 1E5 barcoded MDA-MB-231 cells were implanted to the mammary fat pads to form mammary tumors. 5 weeks later, the mammary tumors were completely removed, and a single dose of 5mg/kg doxycycline was applied to the mice weekly for 5 weeks via I.P. injection. At week 12, tissues with metastatic lesions were dissected and subjected to further analysis.

(E) Heatmap showing the feature matrix of mutation events on barcodes from metastatic lesions of mouse #510.

(F) Body map showing the composition of different basis generated by NMF analysis from mouse #510 and #509 (MDA-MB-231). The value of each basis was transformed from mixture coefficients matrix of 200 NMF runs, and the size of each node indicates the Shannon entropy.

(G) Chord diagrams illustrating the composition flow of barcode mutations between primary tumors and selected metastatic lesions sharing the cluster-unique basis according to the mixture coefficient matrix of NMF analysis in mouse #510 and #509. The length of each

bar indicates the value of Shannon entropy, and the solid proportion represents mutations observed in the primary tumor while the striped proportion represents mutations observed only in metastases. The numbers of mutations in each proportion and flow are noted. Connections with the break indicate the mutations that were not observed in the directly connected lesions but in the primary tumors. See also Figure S4 and Table S1.

Figure 5. Bone-entraining boosts the metastatic capacity of single cell-derived cancer cells.

(A) Experimental design (left) and representative BLI images (right) to test the metastatic capacity of mammary, lung, or bone-entrained single cell derived populations (SCPs). MDA-MB-231 SCP21 cells (Par) were inoculated in mammary fat pad, lung or bone for 4 weeks, and then extracted, and expanded *in vitro* for less than 3 passages. 4 mammary tumors (MFP), 3 lung metastases (LM), and 4 bone metastases (BM) derived SCP21 cells were recovered. 1E5 different organ entrained cells (randomly selected) at passage 3 and parental SCP21 cells were njected into the left ventricle (intra-cardiac injection) of nude mice. The colonization of different organ entrained SCP21 cells was monitored by BLI imaging weekly. N (# of mice) = 8 (Par); 10 (MFP); 15 (BM); 10 (LM).

(B) Comparison of the normalized whole-body bioluminescent intensity at day 7 in animals received same number of MFP-, LM-, BM- or Par-SCP21 cells.

(C) Colonization kinetics of MFP-, LM-, BM- and Par-SCP21 cells after intra-cardiac injection. N (# of mice) = 8 (Par); 10 (MFP); 15 (BM); 10 (LM).

(D) Percentage of ALDH+ stem-like population in MFP-, LM-, BM- and Par-SCP21 cells as determined by flow cytometry.

(E) The histogram (left) and median fluorescent intensity (right) of surface CD44 protein in MFP-, LM-, BM- and Par-SCP21 cells as determined by flow cytometry.

(F) Heat map showing the relative expression level of proteins in Par- and organ-entrained SCP21 cells. The protein levels were quantified and converted into Z-score from three independent western blottings.

(G-I) Representative BLI images (**G**), normalized BLI intensity at day 7 (**H**), and the colonization kinetic (**I**) of MFP-, BM-, and Par- SCP2 cells after I.C. injection. N (# of mice) = 10 (Par); 8 (MFP); 10 (BM).

(J-K) Percentage of ALDH+ population (**J**) and expression of surface CD44 (**K**) in MFP-, BM-, and Par- SCP2 cells by flow cytometry. N (# of replicates) = 3 (**J**); 2 **(K)**.

(L-M) Representative fluorescent images (**L**) and quantification (**M**) of CD44 and ALDH1A1 expression on circulating tumor cells (CTCs) from mice bearing SCP21 cells derived mammary tumors or bone metastases. CTCs were pooled from 5 blood samples. Scale bar, 10 μm.

(N) Expression levels of CD44 mRNA in CTCs from breast cancer patients with bone metastases or other metastases (GSE86978).

P values were determined by Fisher's LSD test following one-way ANOVA test in **B**, **D**, **E**, **H**, and **J**; by Fisher's LSD test post two-way ANOVA test in **C** and **I**; by student t-test in **F**; by Mann-Whitney test in **M** and **N**. See also Figure S5.

Figure 6. Bone-entraining for further dissemination is dependent on EZH2 mediated epigenetic reprograming.

(A) Levels of EZH2 signature genes (GSVA) in bone and other tissue entrained-SCP21 cells.

(B) Levels of EZH2 signature genes in bone entrained-SCP21 cells after different passages of *in vitro* culture. Cells were sub-cultured every 5 days, and 20E4 cells were seeded back to the culture dishes.

(C) Percentage of ALDH1+ population in bone entrained-SCP21 cells at different passages.

(D) Representative western blotting of proteins in bone entrained-SCP21 cells after different passages of *in vitro* culture.

(E-G) The schematic diagram and representative BLI images (**E**), normalized BLI intensity at day 7 (**F**), and the colonization kinetics (**G**) of BM-SCP21 cells with 5-day's EZH2 inhibitor treatment or control cells by intra-cardiac injection. P2 BM-SCP21 cells were treated with 1uM EZH2 inhibitor EPZ011989 (EPZ) for 5 days. Before injection, cells were rinsed with PBS three times to completely remove EPZ. Same number of non-treated BM-SCP21 cells at P3 were used as control. N (# of mice) = 15 (-EPZ); 9 (+EPZ).

(H) Comparison of ALDH1+ cells in EPZ treated and non-treated BM-SCP2 cells as determined by flow cytometry. N (# of replicate) =3.

(I-K) Representative BLI images (**I**), normalized BLI intensity at day 7 (**J**), and the colonization kinetics (**K**) of BM-SCP2 cells with 5-day treatment of EPZ before intra-cardiac injection. Same number of non-treated BM-SCP2 cells at the same passage were used as control. N (# of mice) = 10 (-EPZ); 7 (+EPZ).

(L) Schematic diagram of the experimental design assessing the multi-site metastases from bone lesions with inducible depletion of EZH2 protein. Animals were injected with 1E5 MDA-MB-231 cells stably transduced with inducible shRNAs targeting EZH2 at right hindlimb via IIA injection. One week later, mice were randomly separated into two groups, and given 1mg/ml doxycycline or vehicle in 1% sucrose water for 7 weeks. The metastases were examined at week 8.

(M) Growth kinetic of the primary bone lesions in mice receiving Dox or control water, as determined by *in vivo* bioluminescent imaging. The BLI intensity at right hindlimbs were normalized to the mean value of BLI intensity at the same regions at day 0. N (# of mice) = 10.

(N) Heat map of *ex vivo* BLI intensity and status of metastatic involvement at tissues of animals with EZH2 depleted or control bone metastases.

(O) Models for secondary metastatic dissemination from established bone metastases. Bone resident tumor cells are epigenetically reprogrammed by the bone microenvironment, which leads to the enhanced plasticity and stemness. These bone-entrained metastatic seeds exhibit reduced organo-tropism but increased metastatic capacity to multiple organs, which drives the multi-organ metastases at the terminal stages of cancer progression.

P values were determined by student t-test in **A**, **F**, and **J**; by test for linear trend following repeat measure one-way ANOVA in **B** and **C**; by LSD test following two-way ANOVA in **G**, **K** and **M**; by ratio paired t-test in **H**; by Fisher's exact test on the ratio of metastatic involvement and Mann-Whitney test on BLI intensity in **N**. See also Figure S6.

Supplemental Figure Legends

Supplementary Figure 1. Metastatic spread in animals with established bone metastases, related to Figure 1

(A) Metastatic lesions detected by microCT (lower) or *ex vivo* bioluminescent imaging (upper) in the same bone. Right table showing that 12 in 35 lesions recovered by BLI were not detected by microCT in this study.

(B) Deep imaging of metastases in tissues from mice with primary bone metastases at the right hindlimb. Red, tumor cells; Green, vessels. Scale bar, 100 μm.

(C) H&E staining of metastases across various tissues in mice with IIA-injected bone metastases. Scale bar, 20 μm.

(D-E) Correlation plots showing the correlation between *ex vivo* BLI intensities and the size of metastatic lesions across paired hindlimbs (**D**) or various tissues (**E**) on different animals. The size of metastases refers to the ratio of human genomic contents from tissues of the same weight here. Such ratio was calculated with the Ct values of human HPRT and mouse GAPDH DNA by q-PCR. Spearman correlation r and p value was indicated.

(F) Heat map showing the pattern of metastatic spread in animals with established PC3 or MCF-7 bone lesions via IIA injection. Red cells indicate the presence while gray cell represent the absence of detectable lesions by *ex vivo* BLI imaging. N (# of mice) = 8 (PC3); 8 (MCF-7).

(G) Representative immunofluorescent images of tumor lesions in skeletal tissues and other tissues from animals with intra-femoral injected MDA-MB-231 tumor cells. Red, tumor cells; Green, vessels; Blue, Nucleus. Scale bar, 20 μm.

Supplementary Figure 2. Established bone tumors metastasize more to other tissues, compared to mammary or lung tumors, related to Figure 1.

(A) PET scanning of mammary gland, lung, and hindlimbs of animals with established mammary tumors, lung metastases or bone metastases, respectively.

(B) microCT scanning of the hindlimbs from mice with established mammary tumors, lung metastases, or bone metastases and tumor-free control mice.

(**C-D**) Representative immunofluorescent images of tissues from mice with lung metastases (**C**) or mammary tumors (**D**). Scale bar, 100 μm.

(E-G) Combined bar plot and dot plot showing the tumor burden of primary lesions in different models of MCF-7 (**E**), MDA-MB-231 (**F**) and AT-3 (**G**) cells. The primary lesions refer to the mammary tumors in MFP models, bone metastases in IIA and IF models, and lung metastases in IIV models. Tumor burden were determined with the total *ex vivo* BLI intensity (count/s).

(H) Combined bar plot and dot plot showing the initial tumor burden at lung after injection (d. 0, Left) and the normalized increase of lung tumor burden at the end point (d. 56, Right) in mice with bone or lung metastases.

P values were determined by Dunn's test following Kruskal-Wallis test in **E**, **F** and **G**; by Mann-Whitney test in **H**.

Supplementary Figure 3. Recipient mice parabiotic with mammary tumor-bearing mice show no metastatic spread, related to Figure 3.

(A) Representative *ex vivo* BLI images of tissues from recipient mice in mammary tumor group, in comparison to Figure 3E. 19 animals in total were examined in this group.

(B) Representative immune fluorescent images in search of tumor cells in tissues from recipient mice parabiotic with mice bearing mammary tumors, in comparison to Figure 3G. Tissues from 8 animals were examined. Red, tumor cells; Green, vessels; Blue, Nucleus. Scale bar, 100 μm.

Supplementary Figure 4. Metastatic spread delineated by the evolving barcode system, related to Figure 4

(A) Fluorescence microscopy showing the expression of EGFP-tagged Cas9 protein in barcoded MDA-MB-231 cells with a short term of doxycycline treatment *in vitro*. Red, cancer cells; Green, Cas9-EGFP. Scale Bar, 100μm.

(B) Dot plot showing the barcode diversity in samples from right hindlimb (R.H.), left hindlimb (L.H.) and lung of mice received IIA-injected 10E4 barcoded MDA-MB-231 cells at the right hindlimb. Mice were given a dose of 5mg/kg doxycycline weekly via I.P. injection 2 weeks after IIA injection for 5 weeks. The tissues were collected at week 10. Two mice were examined here.

(C) BLI images of dissected metastatic lesions from mouse #509, #121 and #520 in barcode analysis. Mouse #509 is a nude mouse subjected to the same procedure with mouse #510. Mouse #121 and #520 are C57BL/6J mice implanted with AT-3 tumors. The AT-3 tumors were resected 18 days after implantation, and mice were given a dose of 5mg/kg doxycycline weekly via I.P. injection. The metastatic tissues were dissected at day 42 after tumor implantation for mouse #121 and #520.

(D) Heatmap showing the feature matrix of mutation events in samples from mouse #509, #121 and #520.

(E) Plots of NMF rank survey, consensus matrix, basis components matrix and mixture coefficients matrix of 200 NMF runs on the barcodes from metastatic lesions of four animals.

(F) Body maps showing the transformed composition of basis components in metastatic lesions from mouse #121 and #520 (AT-3).

(G) Chord diagrams illustrating the composition flow of mutation events across primary tumors and selected metastatic lesions with similar basis according to the mixture coefficient matrix of NMF analysis in mouse #121 and #520. The length of each bar indicates the value of Shannon entropy, and the solid proportion represents the mutation events which can be traced in the primary tumor while the striped proportion represents the mutation events observed only in metastases. The numbers of mutation events in each proportion and stream are noted. Connections with a break represent the mutation events that were not observed in the directly connected lesions but the primary tumors.

(H) Correlation plot of Shannon entropy and metastatic burden of lesions as indicated by human genomic content of barcoded MDA-MB-231 samples. Spearman r and p value was indicated.

(I) Correlation plot of Shannon entropy and metastatic burden of lesions as indicated by BLI intensity of barcoded AT-3 samples. Spearman r and p value was indicated.

Supplementary Figure 5. Bone-entrained tumor cells are more metastatic and less organo-tropic, related to Figure 5

(A) Pie chart depicting the major clones in parental SCP21 cells, passage 3 and passage 9 bone-entrained SCP21 cells based on whole exome sequencing (WES) analysis. The

subline of BM-SCP21 cells analyzed was the same subline subjected to *in vivo* study. Single nucleotide variations (SNV) and copy number variations (CNV) were used to evaluate major subclones.

(B-D) The number of metastatic lesions (**B**), tumor burden (**C**) and representative immunofluorescent images (**D**) in non-bone and bone tissues from mice received intracardiac injection of Par-, LM-, or BM-SCP21 cells. Tumor burden on other organs were not compared as few metastases were detected on those sites. N (# of mice) = 8 (Par); 10 (LM); 5(BM). Scale bar, 100 μm.

(E) Representative western blotting images in Par-, MFP-, LM-, and BM-SCP21 cells.

(F) Relative mRNA levels of selected genes in BM-SCP2 and parental SCP2 cells. Blue, Epithelial markers; Orange, Mesenchymal markers or EMT promoters; Black, Epigenetic regulators; Red, Stemness markers. The mRNA levels were determined by qRT-PCR, and then transformed into Z-score. Two replicates in each group were tested. N (# of replicate) = 2.

P values were assessed by Fisher's LSD test following one-way ANOVA test in **B**; by Dunn's test following Kruskal-Wallis in **C**; by student t-test in **F**.

Supplementary Figure 6. Enhanced spread from bone metastases is mediated by EZH2 activity, related to Figure 6

(A) Bar and dot plot showing the change of EZH2 signature in BM-SCP21 cells upon a short period of *in vitro* treatment of EPZ011989.

(B) Bar and dot plot showing the change of ALDH+ population in BM-SCP21 cells upon a short period of *in vitro* treatment of EPZ011989.

(C-D) Representative western blotting images (**D**) and quantification (**E**) in BM-SCP21 cells upon a short period of *in vitro* treatment of EPZ011989.

(E) Quantification of the protein expression levels in BM-SCP21 cells at different passages.

(F) *In vitro* growth kinetic of BM-SCP21 cells with or without 1uM EPZ treatment, shown as the increase of the confluency determined by Incucyte. Same BM-SCP21 cells were subjected to *in vivo* studies. N (# of replicate) = 4.

(G-H) Representative western blotting images (**G**) and quantification (**H**) in MDA-MB-231 cells after depletion of EZH2 protein. Cells were treated with 1μg/ml Doxycycline or PBS for 48 hours *in vitro* to deplete the expression of EZH2.

(I) *In vitro* growth kinetic of MDA-MB-231 cells after knockdown of EZH2. N (# of replicate) = 4.

(J) Confocal imaging of indicated proteins in primary bone lesions of mice received either doxycycline or vehicle. Scale bar, 20 μm.

P values were determined by test for linear trend following repeat measure one-way ANOVA in **E**; ratio paired t-test in **A**, **B**, and **D**; by LSD test following two-way ANOVA in **F** and **I**; by student t-test in **H**.

STAR Methods

CONTACT FOR REAGENT AND RESOURCE SHARING

Further information and requests for resources or reagents should be directed to the lead contact Dr. Xiang H.-F. Zhang at xiangz@bcm.edu

EXPERIMENTAL MODEL AND SUBJECT DETAILS

Cell lines and Cell Culture

Human triple negative breast cancer cell lines MDA-MB-231, human estrogen receptor positive luminal breast cancer cell line MCF-7, human prostate cancer cell line PC-3, and HEK293T cells were obtained from ATCC. SCP21 cells were obtained from Joan Massagué lab. MCF-7 SCPs were generated from single cells of parental MCF-7 cells in the lab. All cells were maintained in DMEM high glucose media supplemented with 10% FBS and 1% penicillin-streptomycin in 5% CO_2 incubator. MCF-7, MDA-MB-231 and their derivative cells were authenticated by the Cytogenetics and Cell Authentication Core at MD Anderson Cancer Center. The mycoplasma contamination was routinely examined in the lab using PlasmoTest™ Mycoplasma Detection Kit (InvivoGen) and no contamination was detected in the cells used in this study. Incucyte (Essen BioScience) was used to assess the growth of cells in culture.

Animals

The *in vivo* studies were covered by and conducted in accordance with a protocol approved by the Baylor College of Medicine Institutional Animal Care and Use Committee. Nude mice [Athymic Nude-Foxn1^{nu}] were purchased from Envigo, while C57BL/6J (stock no. 000664) and immunodeficient NRG (stock no. 007799) mice were from Jackson Laboratories. Age-matched female or male mice of 6- to 8-week-old were used in this study. In tumor models using MCF-7 and SCP2 cells, slow-released estradiol tubes were implanted under the dorsal neck skin of animals one week prior tumor implantation.

METHOD DETAILS

Plasmid Construction

TLCV2 plasmid was a gift from Adam Karpf (Addgene plasmid # 87360). To construct the TLCV2-hgRNA-A26 plasmid, the synthesized hgRNA-A26 oligos were annealed and ligated with BsmBI and EcoRI digested TLCV2 plasmid. The TRIPZ inducible EZH2 shRNA plasmids (Clone ID: V2THS_63066 and V2THS_63067) were purchased from Horizon Discovery Ltd. Plasmids were extracted from the growing bacterial clones and confirmed by Sanger sequencing. The oligo sequences are listed in the Key Resources table.

Lentiviral Production and Transduction

Luciferase/fluorescent protein reporter plasmids, or TRIPZ-shEZH2, or TLCV2-hgRNA-A26 were transfected together with psPAX2 and pMD2.G packaging plasmids into HEK293T cells using X-tremeGENE HP DNA transfection reagent (Sigma). 48 hours later, the supernatant was harvested and filtered by 0.45 um filter (VWR International). Cancer cells were transduced by the fresh lentivirus with 8ug/ml polybrene (Sigma). Two days later, GFP/mRFP positive cells were sorted to generate reporter cell lines. For cells with inducible evolving barcodes or shEZH2, cells were treated with 2 μg/ml puromycin in culture for 10 days before experiments.

Intra-iliac artery, Intra-iliac vein, and Intra-femoral Injection

Both intra-iliac artery and vein injections were performed as previously described (Wang et al., 2015b; Yu et al., 2016). Briefly, animals were anesthetized and restrained on a warming pad. The surgery area was sterilized, and a 7-8 mm incision was made between the right hind limb and abdomen to expose the common iliac vessels. Cancer cells were suspended in 100μl PBS and delivered to the iliac artery or vein by 31G insulin syringe (Becton Dickinson) to generate bone or lung metastases, respectively. For intra-femoral injection, a port through the right femoral plateau was made by a 28G syringe needle into the bone marrow cavity. Then, cancer cells in 20 μl PBS was slowly delivered into the bone marrow cavity.

Mammary Fat Pad, Intra-Ductal and Intra-Cardiac injection

For mammary tumor models, cancer cells mixed 1:1 with growth factor reduced Matrigel Matrix (Corning) were orthotopically implanted into the right fourth mammary fat pad of mice. In the cross-seeding experiment, the mammary tumors were implanted at the fourth left mammary gland immediately after the IIA injection of same number of cancer cells in the right hind limb on the same animal. The intra-ductal injection (or MIND model) was performed as previously reported (Nguyen et al., 2000). Briefly, the tip of the fourth nipples was cut off and cancer cells in 30 ul PBS were directly injected into the exposed duct using 22G blunt needle fitted to a Hamilton syringe. For intra-cardiac injection, cancer cells in 100 μl PBS were directly injected into the left ventricle of anesthetized animals.

Parabiosis and Reverse Procedure

The procedure for parabiosis and reverse procedure were described previously (Kamran et al., 2013). Mice were housed in pairs for at least two weeks to ensure the harmonious cohabitation ahead the surgery. The donor mice were given a tumor implantation surgery on the right side of the body via MFP or IIA injection one week before the parabiosis surgery. During parabiosis surgery, both donor and recipient mice were anesthetized by isoflurane and placed back to back on a warming pad. A longitudinal incision was made on the left side of donor mice and right side of recipient mice starting from the elbow to the knee joints, and then the skin was gently detached from the subcutaneous fascia. The joints between parabiotic pairs were tightly connected with non-absorbable 4-0 suture. The skin incision was then closed side-by-side with absorbable 5-0 suture. The parabiotic pairs were closely monitored until full recovery. 7 weeks after the surgery, a reverse procedure was performed to separate the parabiotic pairs.

Bioluminescence Imaging, Tissue Collection and Quantification of BLI Intensity

In vivo bioluminescence imaging (BLI) was performed weekly with IVIS Lumina II (Advanced Molecular Vision). Briefly, the anesthetized animals were imaged immediately after administration of 100 μl 15 mg/ml D-luciferin (Goldbio) via retro-orbital venous sinus. To ease the comparison across different animals and tissues, the exposure setting was fixed in this study except that the duration of exposure was adjusted to avoid saturation of signals. If not specified, all the animals were sacrificed 8 weeks after the tumor engraftment. At the end point, live animals were given D-Luciferin and immediately dissected. The tissues were examined by *ex vivo* BLI imaging following a fixed order across different animals. The whole process of dissection and *ex vivo* imaging was typically done in less than 15 minutes per animal. The excised tissues were either snap frozen immediately or fixed by 4% PFA at 4 ℃ overnight, cryopreserved with 30% sucrose PBS solution, and then embedded in OCT (Tissue-Tek). For bone tissues, a 7-day decalcification in 14% PH

7.4 EDTA solution was required before embedding. To quantify the metastatic burden, the total BLI flux was calculated over the same region of interest defined for each type of tissues across different animals and presented as total count/s to normalize the influence of exposure duration. Metastatic lesions were defined as the clustered, normally distributed bioluminescent signals above the threshold of 15 counts/pixel under the maximum 120-second exposure.

Small Animal PET-CT Scanning

PET-CT scanning on tumor bearing mice was performed by the Small Animal Imaging Facility (SAIF) core at Baylor College of Medicine. Briefly, animals were fasted for about 12 hours and given with Flourine-18 labeled fluorodeoxyglucose (18F-FDG) one hour before the scanning via intra-peritoneal injection (Cyclotope, Houston, TX). The scanning was performed with appropriate anesthesia and monitoring to maintain normal breathing rates of subjects. Images were acquired by an Inveon scanner (Siemens AG, Knoxville, TN). The parameters of scanning and image analysis were described in the accompanied study (Bado et al., 2019).

Deep Imaging of Intact Tissues

Animals with metastases were retro-orbitally given 1mg 70kDa fluorescein-dextran (Invitrogen) and 10mg Alexa Fluor 488 conjugated anti-mouse CD31 antibody (R&D System) to label vasculatures. 10 minutes afterward, tissues with metastatic lesions were excised under the guide of *ex vivo* BLI imaging. The dissected tissues were then cleaned with cold PBS and fixed in 4% PFA for 4 hours at 4 ℃. To create a window for deep imaging, part of the cortical bones was gently peeled off. Bone tissues were then decalcified at 4 ℃ overnight before next step. Then, tissues were equilibrated in 30% sucrose solution and later in RapiClear® 1.49 (SunJin Lab Co) overnight until the tissues became transparent. The cleared tissues were mounted with RapiClear® 1.49 and Z-stack imaging was performed with a Fluoview FV2000MPE microscope (Olympus). The vasculatures and tumor lesions were reconstructed with Imaris Viewer (Oxford Instrument).

Immunofluorescent Staining

Frozen sections and HE-stained slides were prepared by the Breast Center Pathology Core at Baylor College of Medicine. The immunofluorescent staining was performed with antibodies against mRFP (Rockland, 600-401-379), EGFP (Abcam, 13970), mouse CD31 (R&D Systems, AF3628), and mouse VE-Cadherin (R&D Systems, AF1002). Briefly, the frozen slides were warmed at room temperature for 10 minutes and rinsed with PBS twice. After the penetration with 0.3% Triton X-100 in PBS for 30 minutes, the sections were blocked by 10% donkey serum in PBS-GT (2% Gelatin, 0.1% TritonX-100) for 1 hour at RT. Then the sections were incubated with primary antibodies overnight at 4℃. The next day, the slides were incubated with Alexa Fluor 488 conjugated Donkey anti-Chicken IgY (Jackson ImmunoResearch, 703-546-155), Alexa Fluor 555 conjugated Donkey anti-Rabbit IgG (Thermo Fisher, A31572), and Alexa Fluor 647 conjugated Donkey anti-Goat IgG (Jackson ImmunoResearch, 705-606-147) for 2 hours at RT. The stained sections were then mounted with ProLong™ Gold antifade mountant with DAPI (Thermo Fisher, P36935). Images were acquired by a Zeiss LSM780 confocal microscope, or a Leica DMi8 inverted microscope, or a Zeiss Axioscal.Z1 scanner.

Genomic DNA Extraction from Tissues and Cells

The spatially distinct metastatic lesions were excised and separated with the guide of BLI imaging. The tools were cleaned with 70% isopropanol followed by a bead-sterilizer in between different collections to avoid cross-contamination. The dissected tissues were snap-frozen and stored in -80℃ until next step. For tissues, samples were first homogenized with lysis buffer from Quick-DNA Miniprep Plus Kit (Zymo Research, D4068) by Precellys Lysing Kit (Bertin Instruments, CK14 or MK28-R) on a Precellys Evolution homogenizer (Bertin Instruments). Then, the homogenized tissues or cells were incubated at 55℃ for 3 h and treated with 0.33 mg/mL RNase A at 37℃ for 15 min. Genomic DNA was further extracted using Quick-DNA Miniprep Plus Kit. The final product was assessed by NanoDrop 2000 (Thermo Scientific) and 100 ng DNA from each sample was used in q-PCR to determine the human/mouse DNA ratio with primers specifically targeting human HPRT and mouse Gapdh gene. For the samples that do not reach the threshold at the end of 40 cycles of PCR, a Ct value of 40 cycles was assigned for the calibration of human DNA ratio.

Amplification and Sequencing of hgRNA Barcodes

Barcodes were amplified by two rounds of PCR. The first round of PCR was performed with 100 ng genomic DNA using Platinum Taq DNA Polymerase (Invitrogen) with Barcode-For and Barcode-Rev primers in 15 cycles. The second round of PCR were performed in a real-time setting and stopped in mid-exponential phase using PowerUp SYBR Green Master Mix (Thermo Fisher) with Barcode-P5-For and Barcode-P7-Rev primers. The sequences of primers are provided in Key Resources Table. PCR products were then column-purified with QIAquick PCR purification Kit (QIAGEN) and assessed with Qubit. The NEBNext Multiplex oligos for Illumina (Dual index primer set 1,NEB, E7600S) and the NEB library preparation kit for Illumina (NEB, #E7645S) were used for library preparation as previously described (Kalhor et al., 2017). Barcodes from MDA-MB-231 spontaneous metastases were sequenced on Illumina Hiseq lanes provided by Novogene while other samples were sequenced with NextSeq 500/550 lanes by the Genomic and RNA profiling Core at Baylor College of Medicine.

Evolving Barcode Data Processing

A customized pipeline was used to extract the sequences and counts of barcodes from FASTQ files. Briefly, to identify the barcoding region, the R1 sequence was globally aligned to the A26 reference barcode and annotated using TraceQC package (https://github.com/LiuzLab/TraceQC). The parameters used for alignment are: +2 for match score, -2 for mismatch score, -6 for gap opening penalty and -0.1 for gap extension penalty. Next, the adapter sequences were trimmed off from the annotated sequence. Then, the sequences with alignment scores lower than 200 or with count less than 10 were removed from the subsequent analysis. Barcode sequence from each read was extract, which is 117 bps starting from 58 bp before the predicted TSS. Then the mutation events were categorized by TraceQC from each barcode into 4 attributes: type of mutations, starting position, length of mutation, and the mutant sequence. The mutation events were normalized by the read count per million (RPM) approach and the normalized count was used to generate the feature matrixes for metastases in individual animal. The Shannon entropy of mutation events were calculated using the formula: $H(X) = -\sum_{i=1}^{n} P(x_i) log_2 P(x_i)$.

Non-negative matrix factorization (NMF) analysis

To delineate the phylogenetic relation across metastases of different sites, we performed the NMF analysis on the normalized mutation count matrix using NMF package in R (Gaujoux and Seoighe,

2010). The NMF analysis generate robust clusters on both mutation events and metastatic samples, which can be further interpreted into features shared across clonotypes. Given the dimension of the mutation count matrix, we ran the NMF 200 times to perform the rank survey. To determine the appropriate rank (k) for NMF analysis, in addition to visually examining the clusters, Cophenetic and Silhouette scores were used to quantitatively evaluate the robustness of NMF clusters. The Cophenetic score measures the similarity of two objects to be clustered into one cluster in the consensus matrix. High Cophenetic correlation means the consensus matrix possesses better separated clusters. In mouse 510, k=6, while in mouse 509, k=7 or 8; in mouse 121 and 520, k<5, is the local optimum as shown in the Cophenetic score curve. The Silhouette score was then used to validate the choice of k, as it indicates the similarity of an object to its belonged cluster. The Silhouette scores also evaluate the consistency between the consensus map and the coefficient matrix. Based on the Silhouette curves, k= 6 in mouse 510 while k=7 for mouse 509, k=3 for both mouse 121 and 520 is the local optimum for the consensus matrix in NMF analysis of individual mutation matrix. To enable the reproducibility of the NMF analysis, the final factorization was run with an initial seed on the chosen rank. The body maps were then generated from the values of each basis in a specific metastasis in the mixture coefficient matrix in combined with the Shannon entropy. To illustrate the composition flow of mutations across samples, the count matrix of mutation events was firstly ranked and segmented to enable the most extent of connectivity between two samples by Excel. The value of Shannon entropy was used to decide the direction of flow and was reflected by the bar length in the plots. The elements in the Chord diagrams were proportionally generated by Inkscape to reflect the number of mutation events.

Preparation of Organ-entrained SCPs

SCP21 or SCP2 cells tagged with mRFP and luciferase gene were implanted to the mammary fat pads, hind limbs, or lungs of female nude mice through MFP, IIA or IIV injection, respectively. 6 weeks later, 4 mammary, 3 lung and 4 bone entrained cells were recovered from SCP21 xenografts. For SCP2 cells, two mammary tumors and one bone metastases were recovered. All the animals failed to develop lung metastases after receiving million SCP2 cells through vein injection, so lung-entrained SCP2 cells were not available in this study. mRFP+ tumor cells were then sorted out from the single cell mixture prepared by the tumor dissociation kit (Miltenyi Biotec). For bone metastases, bone marrow was discarded, and the bone fragments were subjected to tumor dissociation kit. The organ-entrained cells were then expanded under regular culture condition, and cryopreserved immediately after reaching confluency, and considered as P1 SCPs. If not specific, cells were sub-cultured every 5 days and most experiments were performed with SCPs at passage 3. The *in vitro* treatment of EPZ011989 was started with BM-SCPs at passage 2 and lasted for 5 days.

Flow Cytometry

Cells were trypsinated at about 80% confluence and the cell concentration was counted. 20E4 cells were resuspended in 1 ml ALDEFUOR™ Assay buffer, and 5 ul of activated substrate was added into the cell suspension. Then, 0.5 ml of the mixture was transferred to another tube with 5 ul DEAB to inactivate the ALDH enzymatic reaction. Both the DEAB and test samples were incubated at 37℃ for 45 min. Other cells were blocked with mouse anti-CD16/32 antibody (Tonbo Biosciences) for 10 minutes and then stained with APC conjugated CD44 antibody (Tonbo Biosciences) on ice for 30 minutes. ALDH+ cells and CD44 expression were then examined with BD LSR Fortessa Analyzer, and analyzed with FlowJo v10.0 (BD). The percentage of ALDH1+

population in test samples was determined with the same gate containing 0.1% positive cells in the corresponding DEAB sample.

RNA and Protein Extraction, qRT-PCR and Western Blotting

Total RNA was extracted from TRIzol™ (Invitrogen) lysed cells by Direct-zol RNA miniPrep Kit (Zymo Research) with an extra step of in-column DNase treatment. For qRT-PCR, cDNA was generated with RevertAid First Strand cDNA synthesis Kit (Thermo Scientific, K1622) with 1 ug of total RNA following the manufacturer's instructions. Real-time PCR was performed with PowerUp SYBR Green Master Mix (Thermo Fisher) on Biorad CFX Real-Time system. The expression levels of GAPDH mRNA were served as the internal control. The primer sequences are listed in the Key Resources Table. For western blotting, cells were directly scratched from the culture dishes and lysed with RIPA buffer. 20 μg of total proteins were used for electrophoresis with NuPAGE® Novex® Gel system (Invitrogen). Proteins were then transferred to a nitrocellulose membrane using iBlot™ Transfer System (Invitrogen). The membrane was blocked with 5% BSA and incubated with primary antibodies overnight at 4℃. The next day, membranes were incubated with secondary antibodies (LI-COR Bioscience) and scanned by the Odyssey® infrared imaging system.

RNA-Sequencing and Whole Exome Sequencing

mRNA sequencing, read mapping, normalization and quantification were performed by Novogene. One biological replicate from mammary fat pad group failed the quality check and was excluded from the subsequent analysis. EZH2 signature were calculated as the average expression of EZH2-suppressed genes (MSigDB geneset: LU_EZH2_TARGETS_DN) (Lu et al., 2010). Whole exome sequencing was performed by the Genomic and RNA profiling Core at Baylor College of Medicine with a 100X coverage. The pipeline to delineate the clonal structure of SCP21 sublines was describe in the accompany study (Bado et al., 2019) . These were carried out in R environment.

Capture and Staining of CTCs

500μl blood were draw from the right ventricle of anesthetized NRG mice inoculated with mammary tumors or bone metastases after 6 weeks. Blood samples were immediately mixed with 8 ml of red blood cell lysis buffer and incubated on ice for 10 minutes. Samples were then centrifuged at 250 g for 10 minutes at 4℃ and the supernatant was discarded. The same steps were repeated once to completely remove red blood cells. Cell pellets were then re-suspended with cold PBS and transferred to poly-L-lysine coated slides. The slides were placed in the 37℃ incubator for 30 minutes, and fixed with 4% PFA for 10 minutes. Fixed cells were rinsed with PBS for three times, and permeated with 0.3% Triton-X 100 for 30 minutes at RT. Slides were then blocked with donkey serum (Sigma) and anti-mouse CD16/32 antibody (Tonbo Biosciences) for 2 hours and incubated with fluorescence conjugated primary antibodies at 4 ℃ overnight. The next day, slides were stained with Hoechst 33342 and mounted with Prolong™ Diamond Antifade Mountant (Molecular Probe). Circulating tumor cells were identified by a CyteFinder® instrument (Rarecyte) and the images were captured with same exposure setting.

Image Processing and Statistical Test

Immunofluorescent images were first exported by ZEN (Zeiss), or LAS X (Leica Microsystem). The exported images were then analyzed and quantified by Fiji. If not specified, all the data were

generated by GraphPad Prism 8. The statistical analysis was also performed by GraphPad Prism 8 and noted in the corresponding legend. All tests were performed in two-sided test.

Data and Code Availability

The raw data of mRNA sequencing, WES sequencing and barcode sequencing are available in NIH Gene Expression Omnibus with the accession number GSE160773, GSE161181 and GSE161145. The GEO reference series GSE161146 connects all the datasets. The TraceQC package can be found at https://github.com/LiuzLab/TraceQC. The code of NMF analysis of barcode data can be found at https://github.com/LiuzLab/CRISPR_bone_metastasis-manuscript.

Supplementary Table 1. Summary of metastatic lesions and parental tumors with evolving barcode, related to Figure 4.

Sample ID	Mouse ID	Tumor Cells	BLI Flux (Count/s)	Human Genomic Context	Shannon Entropy	QC
510 Tumor	510	MDA-MB-231	N.A.	0.363661292	6.808292	Passed
510 Lung-1	510	MDA-MB-231	24220.00	0.004066884	2.615788	Passed
510 Lung-2	510	MDA-MB-231	38805.00	0.006432119	4.377654	Passed
510 Lung-3	510	MDA-MB-231	62700.00	0.012254848	4.203264	Passed
510 Liver-2	510	MDA-MB-231	542.42	0.000186003	5.003666	Passed
510 Liver-3	510	MDA-MB-231	657.67	0.000209698	1.734293	Passed
510 Liver-5	510	MDA-MB-231	230850.00	0.045450599	4.75026	Passed
510 Liver-6	510	MDA-MB-231	688.83	0.000351357	3.523702	Passed
510 Spleen	510	MDA-MB-231	351.08	2.08879E-06	4.213165	Passed
510 Kidney R	510	MDA-MB-231	18.63	2.78901E-06	1.900215	Passed
510 Kidney L	510	MDA-MB-231	18.68	4.54967E-05	4.553258	Passed
510 Brain	510	MDA-MB-231	13.12	4.42487E-05	3.814387	Passed
510 Hindlimb R	510	MDA-MB-231	12.74	2.0541E-06	4.691222	Passed
510 Hindlimb L1	510	MDA-MB-231	84.25	1.99125E-05	1.413465	Passed
510 Hindlimb L2	510	MDA-MB-231	63.01	1.84344E-06	3.648549	Passed
510 Hindlimb L3	510	MDA-MB-231	118.00	4.97334E-05	1.644237	Passed
510 Forelimb R1	510	MDA-MB-231	246.83	0.000430696	3.586954	Passed
510 Forelimb R2	510	MDA-MB-231	141.58	7.12933E-05	2.026557	Passed
510 Forelimb L1	510	MDA-MB-231	106.92	2.34455E-05	2.143473	Passed
510 Forelimb L2	510	MDA-MB-231	57.63	1.85076E-06	2.548304	Passed
510 Sternum 1	510	MDA-MB-231	204200.00	0.052432473	1.583296	Passed
510 Sternum 2	510	MDA-MB-231	1841.67	0.00042787	4.406749	Passed
510 Spine-1	510	MDA-MB-231	508500.00	0.356310893	1.573945	Passed
510 Spine-2	510	MDA-MB-231	9795.00	0.001214516	1.770436	Passed
510 Ribs R1	510	MDA-MB-231	84900.00	0.054168771	2.26127	Passed
510 Ribs R2	510	MDA-MB-231	18608.33	0.002971289	0.80087	Passed
510 Ribs R3	510	MDA-MB-231	10358.33	0.001858483	2.183824	Passed
510 Ribs L1	510	MDA-MB-231	77000.00	0.01746907	4.537818	Passed
510 Ribs L2	510	MDA-MB-231	12308.33	0.00213605	0.754439	Passed
510 Ribs L3	510	MDA-MB-231	17100.00	0.004434681	1.948894	Passed
510 Skull 1	510	MDA-MB-231	131.17	9.87858E-05	2.1703	Passed
510 Skull 2	510	MDA-MB-231	99.92	5.08726E-05	1.079339	Passed
510 Skull 3	510	MDA-MB-231	46.68	2.80563E-05	1.431532	Passed
509 Tumor	509	MDA-MB-231	N.A.	0.674722739	5.655339	Passed

509 Lung R	509	MDA-MB-231	69800.00	0.004554073	4.223553	Passed
509 Lung L	509	MDA-MB-231	275450.00	0.027209733	3.156388	Passed
509 Liver-1	509	MDA-MB-231	177800.00	0.055610442	4.745565	Passed
509 Liver-2	509	MDA-MB-231	693.58	0.000153578	0.98891	Passed
509 Liver-3	509	MDA-MB-231	557.58	2.39505E-05	2.954312	Passed
509 Liver-4	509	MDA-MB-231	285.17	1.28152E-06	5.516063	Passed
509 Liver-5	509	MDA-MB-231	880.83	0.000123482	2.064823	Passed
509 Spleen	509	MDA-MB-231	122.83	1.57263E-05	3.087503	Passed
509 Kidney R	509	MDA-MB-231	118.50	2.05712E-05	1.986253	Passed
509 Kidney L	509	MDA-MB-231	77.46	1.07733E-06	2.506725	Passed
509 Brain-1	509	MDA-MB-231	168.17	3.87658E-06	0.737711	Passed
509 Brain-2	509	MDA-MB-231	142.58	0.000015433	5.176913	Passed
509 Hindlimb-R	509	MDA-MB-231	26.91	1.13399E-06	1.921928	Passed
509 Hindlimb-L	509	MDA-MB-231	366.42	6.01775E-05	4.956159	Passed
509 Forelimb-R	509	MDA-MB-231	57.73	2.33802E-05	2.494279	Passed
509 Forelimb-L	509	MDA-MB-231	930.00	0.000128635	2.870507	Passed
509 Sternum-1	509	MDA-MB-231	22850.00	0.018928262	3.530393	Passed
509 Sternum-2	509	MDA-MB-231	27183.33	0.021703433	4.186927	Passed
509 Spine-1	509	MDA-MB-231	206150.00	0.033218198	2.28122	Passed
509 Spine-2	509	MDA-MB-231	10691.67	0.000871895	3.443229	Passed
509 Ribs-R1	509	MDA-MB-231	63400.00	0.04111563	1.459806	Passed
509 Ribs-R2	509	MDA-MB-231	57083.33	0.037684392	2.723121	Passed
509 Ribs-R3	509	MDA-MB-231	39566.67	0.017959928	0.438707	Passed
509 Ribs-R4	509	MDA-MB-231	26416.67	0.014761718	0.691731	Passed
509 Ribs-L1	509	MDA-MB-231	53091.67	0.011326675	3.159309	Passed
509 Ribs-L2	509	MDA-MB-231	24591.67	0.006019311	2.87936	Passed
509 Skull-1	509	MDA-MB-231	439.00	0.000162831	3.135177	Passed
509 Skull-2	509	MDA-MB-231	228.00	9.57688E-05	2.590998	Passed
509 Skull-3	509	MDA-MB-231	50.93	5.78161E-05	2.228149	Passed
121 Tumor	121	AT-3	N.A.	N.A.	6.584591	Passed
121 Lung	121	AT-3	25.1	N.A.	6.144102	Passed
121 Liver-1	121	AT-3	64.26667	N.A.	6.129854	Passed
121 Liver-5	121	AT-3	96.25	N.A.	6.103778	Passed
121 Kidney-L	121	AT-3	11.24167	N.A.	6.393486	Passed
121 Spleen	121	AT-3	5.229167	N.A.	6.327988	Passed
121 HL-R	121	AT-3	3.076667	N.A.	5.648208	Passed
121 HL-L	121	AT-3	6.775833	N.A.	4.122812	Passed
121 FL-R	121	AT-3	13.71667	N.A.	4.327983	Passed
121 Ribs-L	121	AT-3	1515.833	N.A.	4.478489	Passed
520 Tumor	520	AT-3	N.A.	N.A.	6.714454	Passed
520 Lung-1	520	AT-3	6245	N.A.	6.620857	Passed
520 Lung-2	520	AT-3	1610.5	N.A.	6.561824	Passed
520 Liver-1	520	AT-3	318.1667	N.A.	6.628045	Passed

520 Liver-2	520	AT-3	179.5833	N.A.	6.611371	Passed
520 Liver-3	520	AT-3	44.85	N.A.	5.810843	Passed
520 Kidney-R	520	AT-3	42.59167	N.A.	4.167957	Passed
520 Kidney-L	520	AT-3	52.475	N.A.	5.339619	Passed
520 Spleen-1	520	AT-3	516.1667	N.A.	6.023512	Passed
520 Spleen-2	520	AT-3	217.75	N.A.	5.219024	Passed
520 HL-R1	520	AT-3	6300	N.A.	5.487375	Passed
520 HL-R2	520	AT-3	5035	N.A.	5.976172	Passed
520 HL-L	520	AT-3	5.516667	N.A.	4.611148	Passed
520 FL-R	520	AT-3	12.45833	N.A.	3.665072	Passed
520 FL-L	520	AT-3	16.64167	N.A.	4.975205	Passed
520 Ribs-L	520	AT-3	31.76667	N.A.	6.567661	Passed
520 Ribs-R	520	AT-3	1284.166667	N.A.	N.A.	Failed
520 Sternum-1	520	AT-3	44.86667	N.A.	6.556045	Passed
520 Sternum-2	520	AT-3	35.91667	N.A.	6.638064	Passed
520 Skull	520	AT-3	4.763333333	N.A.	N.A.	Failed

REFERENCES

Aceto, N., Bardia, A., Wittner, B.S., Donaldson, M.C., O'Keefe, R., Engstrom, A., Bersani, F., Zheng, Y., Comaills, V., Niederhoffer, K., et al. (2018). AR expression in breast cancer CTCs associates with bone metastases. Mol. Cancer Res. *16*, 720–727.

Anwar, T., Arellano-Garcia, C., Ropa, J., Chen, Y.C., Kim, H.S., Yoon, E., Grigsby, S., Basrur, V., Nesvizhskii, A.I., Muntean, A., et al. (2018). P38-mediated phosphorylation at T367 induces EZH2 cytoplasmic localization to promote breast cancer metastasis. Nat. Commun. *9*, 1–13.

Bado, I.L., Wang, H., Poonam, S., Liu, J., Wu, W., Zhang, W., Lo, H.-C., Muscarella, A.M., Janghorban, M., Kim, I.S., et al. (2019). Phenotypic plasticity of ER+ breast cancer in the bone microenvironment. Submitted.

Bos, P.D., Zhang, X.H.F., Nadal, C., Shu, W., Gomis, R.R., Nguyen, D.X., Minn, A.J., Van De Vijver, M.J., Gerald, W.L., Foekens, J.A., et al. (2009). Genes that mediate breast cancer metastasis to the brain. Nature *459*, 1005–1009.

Boyce, B.F., Yoneda, T., and Guise, T.A. (1999). Factors regulating the growth of metastatic cancer in bone. Endocr. Relat. Cancer *6*, 333–347.

Brown, D., Smeets, D., Székely, B., Larsimont, D., Marcell Szász, A., Adnet, P.-Y., Rothé, F., Rouas, G., Nagy, Z.I., Faragó, Z., et al. (2017). Phylogenetic analysis of metastatic progression in breast cancer using somatic mutations and copy number aberrations. Nat. Commun. *8*.

Chang, C.J., Yang, J.Y., Xia, W., Chen, C. Te, Xie, X., Chao, C.H., Woodward, W.A., Hsu, J.M., Hortobagyi, G.N., and Hung, M.C. (2011). EZH2 promotes expansion of breast tumor initiating cells through activation of RAF1-β-catenin signaling. Cancer Cell *19*, 86–100.

Coleman, R.E. (2006). Clinical features of metastatic bone disease and risk of skeletal morbidity. Clin. Cancer Res. *12*, 6243s–6249s.

Coleman, R.E., and Rubens, R.D. (1987). The clinical course of bone metastases from breast cancer. Br. J. Cancer *55*, 61–66.

Coleman, R.E., Smith, P., and Rubens, R.D. (1998). Clinical course and prognostic factors following bone recurrence from breast cancer. Br. J. Cancer.

Coleman, R.E., Guise, T.A., Lipton, A., Roodman, G.D., Berenson, J.R., Body, J.J., Boyce, B.F., Calvi, L.M., Hadji, P., McCloskey, E. V., et al. (2008). Advancing treatment for metastatic bone cancer: Consensus recommendations from the second cambridge conference. Clin. Cancer Res.

Deroose, C.M., De, A., Loening, A.M., Chow, P.L., Ray, P., Chatziioannou, A.F., and Gambhir, S.S. (2007). Multimodality imaging of tumor xenografts and metastases in mice with combined small-animal PET, small-animal CT, and bioluminescence imaging.

DiSibio, G., and French, S.W. (2008). Metastatic patterns of cancers : Results from a large autopsy study. Arch. Pathol. Lab. Med. *132*, 931–939.

Esposito, M., Guise, T., and Kang, Y. (2018). The biology of bone metastasis. Cold Spring Harb. Perspect. Med. *8*.

Gaujoux, R., and Seoighe, C. (2010). A flexible R package for nonnegative matrix factorization. BMC Bioinformatics *11*, 367.

Ghajar, C.M., Peinado, H., Mori, H., Matei, I.R., Evason, K.J., Brazier, H., Almeida, D., Koller, A., Hajjar, K.A., Stainier, D.Y.R., et al. (2013). The perivascular niche regulates breast tumour dormancy. Nat. Cell Biol. *15*, 807–817.

Gonzalez, M.E., Moore, H.M., Li, X., Toy, K.A., Huang, W., Sabel, M.S., Kidwell, K.M., and Kleer, C.G. (2014). EZH2 expands breast stem cells through activation of NOTCH1 signaling. Proc. Natl. Acad. Sci. U. S. A. *111*, 3098–3103.

Gundem, G., Van Loo, P., Kremeyer, B., Alexandrov, L.B., Tubio, J.M.C., Papaemmanuil, E., Brewer, D.S., Kallio, H.M.L., Högnäs, G., Annala, M., et al. (2015). The evolutionary history of lethal metastatic prostate cancer. Nature *520*, 353–357.

Gupta, P.B., Pastushenko, I., Skibinski, A., Blanpain, C., and Kuperwasser, C. (2019). Phenotypic Plasticity: Driver of Cancer Initiation, Progression, and Therapy Resistance. Cell Stem Cell.

Hirukawa, A., Smith, H.W., Zuo, D., Dufour, C.R., Savage, P., Bertos, N., Johnson, R.M., Bui, T., Bourque, G., Basik, M., et al. (2018). Targeting EZH2 reactivates a breast cancer subtype-specific anti-metastatic transcriptional program. Nat. Commun. *9*, 1–15.

Juárez, P., and Guise, T.A. (2011). TGF-β in cancer and bone: Implications for treatment of bone metastases. Bone *48*, 23–29.

Kalhor, R., Mali, P., and Church, G.M. (2017). Rapidly evolving homing CRISPR barcodes. Nat. Methods *14*, 195–200.

Kalhor, R., Kalhor, K., Mejia, L., Leeper, K., Graveline, A., Mali, P., and Church, G.M. (2018). Developmental barcoding of whole mouse via homing CRISPR. Science (80-.).

Kamran, P., Sereti, K.-I., Zhao, P., Ali, S.R., Weissman, I.L., and Ardehali, R. (2013). Parabiosis in Mice: A Detailed Protocol. J. Vis. Exp.

Kang, Y., Siegel, P.M., Shu, W., Drobnjak, M., Kakonen, S.M., Cordon-Cardo, C., Guise, T.A., and Massague, J. (2003). A multigenic program mediating breast cancer metastasis to bone. Cancer Cell *3*, 537–549.

Kennecke, H., Yerushalmi, R., Woods, R., Cheang, M.C.U., Voduc, D., Speers, C.H., Nielsen, T.O., and Gelmon, K. (2010). Metastatic behavior of breast cancer subtypes. J. Clin. Oncol. *28*, 3271–3277.

Kim, M.Y., Oskarsson, T., Acharyya, S., Nguyen, D.X., Zhang, X.H.F., Norton, L., and Massagué, J. (2009). Tumor Self-Seeding by Circulating Cancer Cells. Cell *139*, 1315–1326.

Kingsley, L.A., Fournier, P.G.J., Chirgwin, J.M., and Guise, T.A. (2007). Molecular biology of bone metastasis. Mol. Cancer Ther. *6*, 2609–2617.

Kottakis, F., Polytarchou, C., Foltopoulou, P., Sanidas, I., Kampranis, S.C., and Tsichlis, P.N. (2011). FGF-2 Regulates Cell Proliferation, Migration, and Angiogenesis through an NDY1/KDM2B-miR-101-EZH2 Pathway. Mol. Cell *43*, 285–298.

Lu, C., Han, H.D., Mangala, L.S., Ali-Fehmi, R., Newton, C.S., Ozbun, L., Armaiz-Pena, G.N., Hu, W., Stone, R.L., Munkarah, A., et al. (2010). Regulation of tumor angiogenesis by EZH2. Cancer Cell *18*, 185–197.

Ma, A., Stratikopoulos, E., Park, K.S., Wei, J., Martin, T.C., Yang, X., Schwarz, M., Leshchenko, V., Rialdi, A., Dale, B., et al. (2020). Discovery of a first-in-class EZH2 selective degrader. Nat. Chem. Biol. *16*, 214–222.

Minn, A.J., Kang, Y., Serganova, I., Gupta, G.P., Giri, D.D., Doubrovin, M., Ponomarev, V., Gerald, W.L., Blasberg, R., and Massague, J. (2005). Distinct organ-specific metastatic potential of individual breast cancer cells and primary tumors. J. Clin. Invest. *115*, 44–55.

Nguyen, D.-A., Beeman, N., Lewis, M., Schaack, J., and Neville, M.C. (2000). Intraductal Injection into the Mouse Mammary Gland. In Methods in Mammary Gland Biology and Breast Cancer Research, (Boston, MA: Springer US), pp. 259–270.

Peinado, H., Zhang, H., Matei, I.R., Costa-Silva, B., Hoshino, A., Rodrigues, G., Psaila, B., Kaplan, R.N., Bromberg, J.F., Kang, Y., et al. (2017). Pre-metastatic niches: organ-specific homes for metastases. Nat. Rev. Cancer *17*, 302–317.

Price, T.T., Burness, M.L., Sivan, A., Warner, M.J., Cheng, R., Lee, C.H., Olivere, L., Comatas,

K., Magnani, J., Kim Lyerly, H., et al. (2016). Dormant breast cancer micrometastases reside in specific bone marrow niches that regulate their transit to and from bone. Sci. Transl. Med. *8*, 340ra73.

Qiao, Y., Kang, K., Giannopoulou, E., Fang, C., and Ivashkiv, L.B. (2016). IFN-γ Induces Histone 3 Lysine 27 Trimethylation in a Small Subset of Promoters to Stably Silence Gene Expression in Human Macrophages. Cell Rep. *16*, 3121–3129.

Sflomos, G., Dormoy, V., Metsalu, T., Jeitziner, R., Battista, L., Scabia, V., Raffoul, W., Delaloye, J.-F., Treboux, A., Fiche, M., et al. (2016). A Preclinical Model for ERα-Positive Breast Cancer Points to the Epithelial Microenvironment as Determinant of Luminal Phenotype and Hormone Response. Cancer Cell *29*, 407–422.

Smid, M., Wang, Y., Zhang, Y., Sieuwerts, A.M., Yu, J., Klijn, J.G., Foekens, J.A., and Martens, J.W. (2008). Subtypes of breast cancer show preferential site of relapse. Cancer Res. *68*, 3108–3114.

Ullah, I., Karthik, G.M., Alkodsi, A., Kjällquist, U., Stålhammar, G., Lövrot, J., Martinez, N.F., Lagergren, J., Hautaniemi, S., Hartman, J., et al. (2018). Evolutionary history of metastatic breast cancer reveals minimal seeding from axillary lymph nodes. J. Clin. Invest.

Vanharanta, S., and Massague, J. (2013). Origins of metastatic traits. Cancer Cell *24*, 410–421.

Wang, H., Yu, C., Gao, X., Welte, T., Muscarella, A.M., Tian, L., Zhao, H., Zhao, Z., Du, S., Tao, J., et al. (2015a). The osteogenic niche promotes early-stage bone colonization of disseminated breast cancer cells. Cancer Cell *27*, 193–210.

Wang, H., Yu, C., Gao, X., Welte, T., Muscarella, A.M., Tian, L., Zhao, H., Zhao, Z., Du, S., Tao, J., et al. (2015b). The Osteogenic Niche Promotes Early-Stage Bone Colonization of Disseminated Breast Cancer Cells. Cancer Cell *27*, 193–210.

Wang, H., Tian, L., Liu, J., Goldstein, A., Bado, I., Zhang, W., Arenkiel, B.R., Li, Z., Yang, M., Du, S., et al. (2018). The osteogenic niche is a calcium reservoir of bone micrometastases and confers unexpected therapeutic vulnerability. Cancer Cell *34*, 1–17.

Waning, D.L., Mohammad, K.S., Reiken, S., Xie, W., Andersson, D.C., John, S., Chiechi, A., Wright, L.E., Umanskaya, A., Niewolna, M., et al. (2015). Excess TGF-β mediates muscle weakness associated with bone metastases in mice. Nat. Med. *21*, 1262–1271.

Weilbaecher, K.N., Guise, T.A., and McCauley, L.K. (2011). Cancer to bone: a fatal attraction. Nat. Rev. Cancer *11*, 411–425.

Ye, X., and Weinberg, R.A. (2015). Epithelial-Mesenchymal Plasticity: A Central Regulator of Cancer Progression. Trends Cell Biol.

Yu, C., Wang, H., Muscarella, A., Goldstein, A., Zeng, H.-C., Bae, Y., Lee, B.H.I., and Zhang, X.H.-F. (2016). Intra-iliac Artery Injection for Efficient and Selective Modeling of Microscopic Bone Metastasis. J. Vis. Exp. 1–7.

Yue, Z., Chen, J., Lian, H., Pei, J., Li, Y., Chen, X., Song, S., Xia, J., Zhou, B., Feng, J., et al. (2019). PDGFR-β Signaling Regulates Cardiomyocyte Proliferation and Myocardial Regeneration. Cell Rep. *28*, 966–978.e4.

Zhang, L., Yao, J., Wei, Y., Zhou, Z., Li, P., Qu, J., Badu-Nkansah, A., Yuan, X., Huang, Y.W., Fukumura, K., et al. (2020). Blocking immunosuppressive neutrophils deters pY696-EZH2–driven brain metastases. Sci. Transl. Med. *12*, 5387.

Zhang, X.H.F., Jin, X., Malladi, S., Zou, Y., Wen, Y.H., Brogi, E., Smid, M., Foekens, J.A., and Massagué, J. (2013). Selection of bone metastasis seeds by mesenchymal signals in the primary tumor stroma. Cell *154*, 1060–1073.

Zhao, E., Maj, T., Kryczek, I., Li, W., Wu, K., Zhao, L., Wei, S., Crespo, J., Wan, S., Vatan, L., et al. (2016). Cancer mediates effector T cell dysfunction by targeting microRNAs and EZH2 via glycolysis restriction. Nat. Immunol. *17*, 95–103.

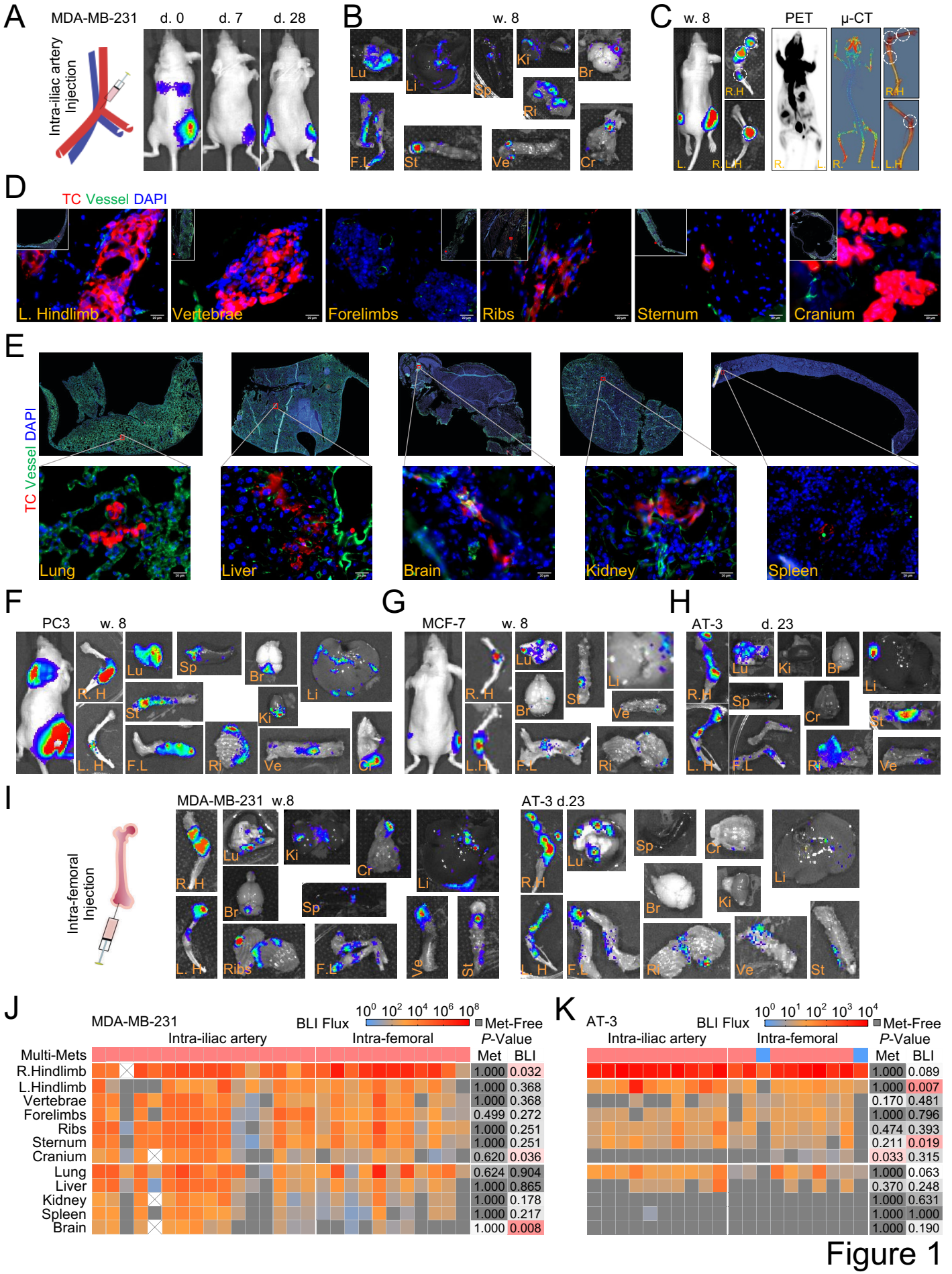
A
MDA-MB-231
d. 0
d. 7
d. 28
Intra-iliac artery Injection
B
w. 8
Lu
Li
Sp
Ki
Br
Ri
F.L
St
Ve
Cr
C
w. 8
PET
μ-CT
R.H
L.H
D
TC Vessel DAPI
L. Hindlimb
Vertebrae
Forelimbs
Ribs
Sternum
Cranium
E
TC Vessel DAPI
Lung
Liver
Brain
Kidney
Spleen
F
PC3
w. 8
G
MCF-7
w. 8
H
AT-3
d. 23
I
Intra-femoral Injection
MDA-MB-231 w.8
AT-3 d.23
J
MDA-MB-231
BLI Flux
Met-Free
Intra-iliac artery
Intra-femoral
P-Value
Met
BLI
Multi-Mets
R.Hindlimb 1.000 0.032
L.Hindlimb 1.000 0.368
Vertebrae 1.000 0.368
Forelimbs 0.499 0.272
Ribs 1.000 0.251
Sternum 1.000 0.251
Cranium 0.620 0.036
Lung 0.624 0.904
Liver 1.000 0.865
Kidney 1.000 0.178
Spleen 1.000 0.217
Brain 1.000 0.008
K
AT-3
BLI Flux
Met-Free
Intra-iliac artery
Intra-femoral
P-Value
Met
BLI
1.000 0.089
1.000 0.007
0.170 0.481
1.000 0.796
0.474 0.393
0.211 0.019
0.033 0.315
1.000 0.063
0.370 0.248
1.000 0.631
1.000 1.000
1.000 0.190

Figure 1

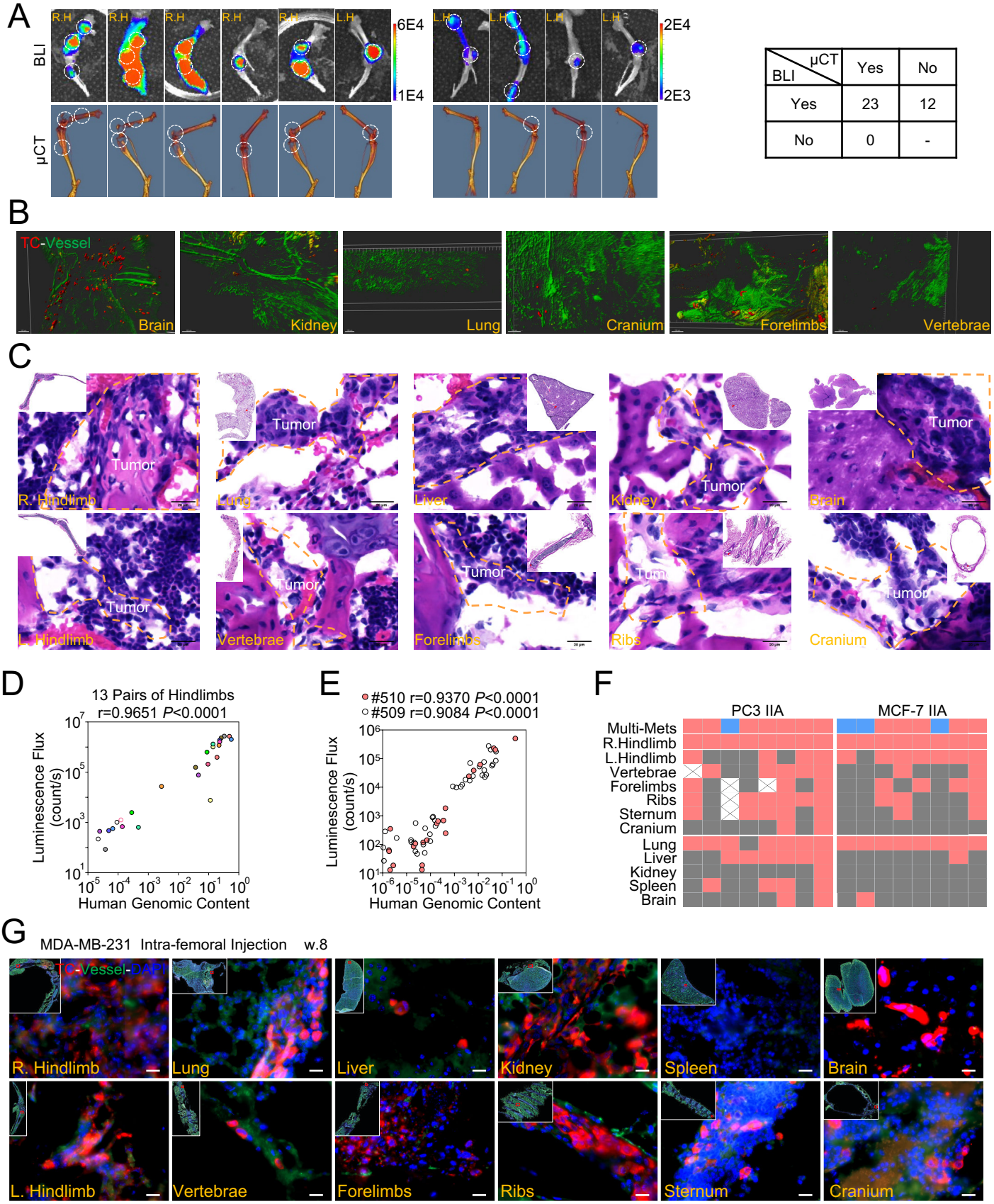

BLI \ μCT	Yes	No
Yes	23	12
No	0	-

Figure S1

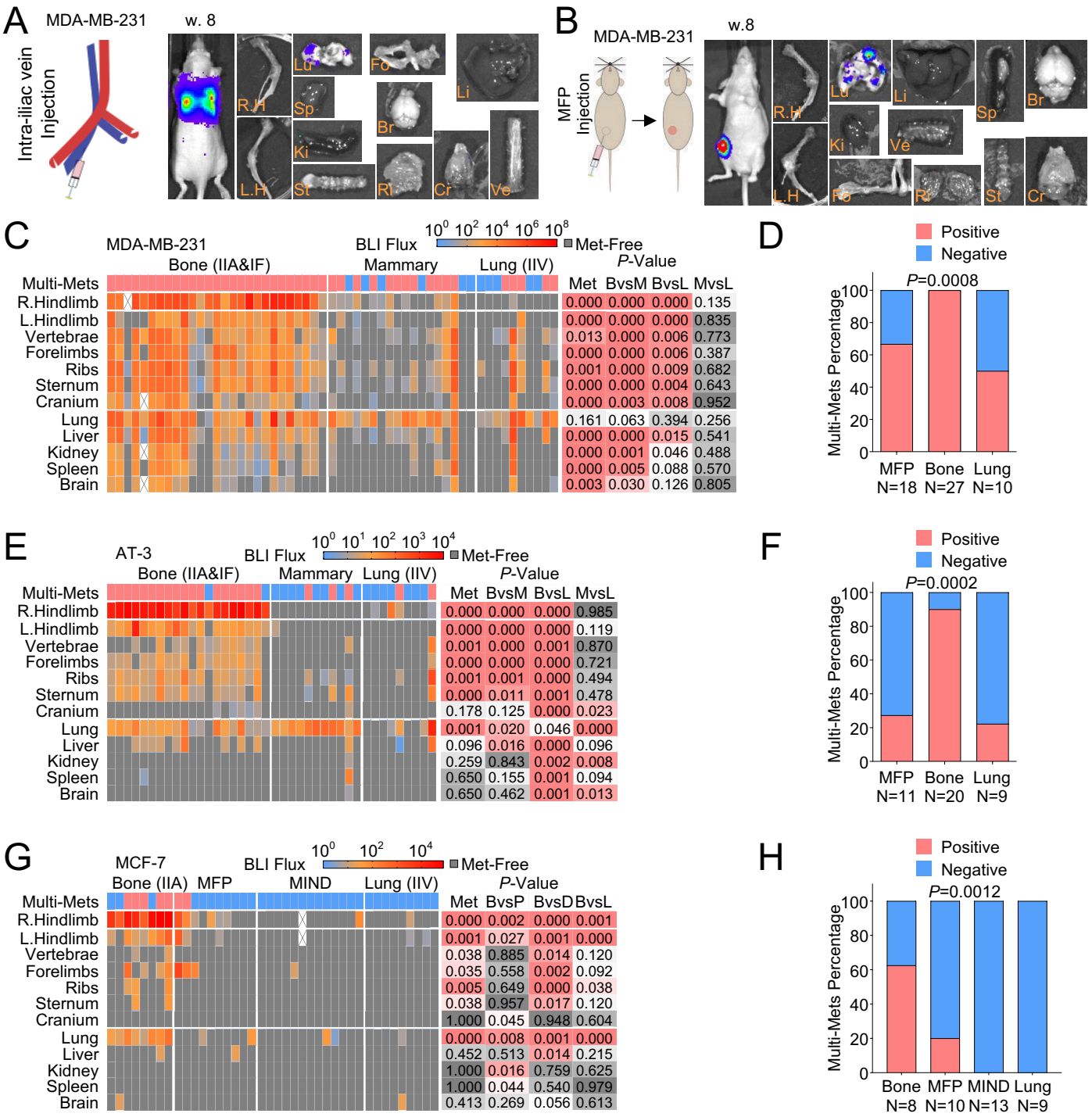
A
MDA-MB-231
w. 8
Intra-iliac vein Injection
R.H
L.H
Lu
Sp
Ki
St
Fo
Br
Ri
Cr
Li
Ve
B
MDA-MB-231
w.8
MFP Injection
C
MDA-MB-231
BLI Flux
Met-Free
Bone (IIA&IF)
Mammary
Lung (IIV)
P-Value
Multi-Mets 0.000 0.000 0.000 0.135
R.Hindlimb 0.000 0.000 0.000 0.835
L.Hindlimb 0.013 0.000 0.006 0.773
Vertebrae 0.000 0.000 0.006 0.387
Forelimbs 0.001 0.000 0.009 0.682
Ribs 0.000 0.000 0.004 0.643
Sternum 0.000 0.003 0.008 0.952
Cranium 0.161 0.063 0.394 0.256
Lung 0.000 0.000 0.015 0.541
Liver 0.000 0.001 0.046 0.488
Kidney 0.000 0.005 0.088 0.570
Spleen 0.003 0.030 0.126 0.805
Brain
Met BvsM BvsL MvsL
D
Positive
Negative
P=0.0008
Multi-Mets Percentage
MFP N=18
Bone N=27
Lung N=10
E
AT-3
BLI Flux
Met-Free
Bone (IIA&IF)
Mammary
Lung (IIV)
P-Value
Multi-Mets 0.000 0.000 0.000 0.985
R.Hindlimb 0.000 0.000 0.000 0.119
L.Hindlimb 0.001 0.000 0.001 0.870
Vertebrae 0.000 0.000 0.000 0.721
Forelimbs 0.001 0.001 0.000 0.494
Ribs 0.000 0.011 0.001 0.478
Sternum 0.178 0.125 0.000 0.023
Cranium 0.001 0.020 0.046 0.000
Lung 0.096 0.016 0.000 0.096
Liver 0.259 0.843 0.002 0.008
Kidney 0.650 0.155 0.001 0.094
Spleen 0.650 0.462 0.001 0.013
Brain
Met BvsM BvsL MvsL
F
Positive
Negative
P=0.0002
Multi-Mets Percentage
MFP N=11
Bone N=20
Lung N=9
G
MCF-7
BLI Flux
Met-Free
Bone (IIA)
MFP
MIND
Lung (IIV)
P-Value
Multi-Mets 0.000 0.002 0.000 0.001
R.Hindlimb 0.001 0.027 0.001 0.000
L.Hindlimb 0.038 0.885 0.014 0.120
Vertebrae 0.035 0.558 0.002 0.092
Forelimbs 0.005 0.649 0.000 0.038
Ribs 0.038 0.957 0.017 0.120
Sternum 1.000 0.045 0.948 0.604
Cranium 0.000 0.008 0.001 0.000
Lung 0.452 0.513 0.014 0.215
Liver 1.000 0.016 0.759 0.625
Kidney 1.000 0.044 0.540 0.979
Spleen 0.413 0.269 0.056 0.613
Brain
Met BvsP BvsD BvsL
H
Positive
Negative
P=0.0012
Multi-Mets Percentage
Bone N=8
MFP N=10
MIND N=13
Lung N=9

Figure 2

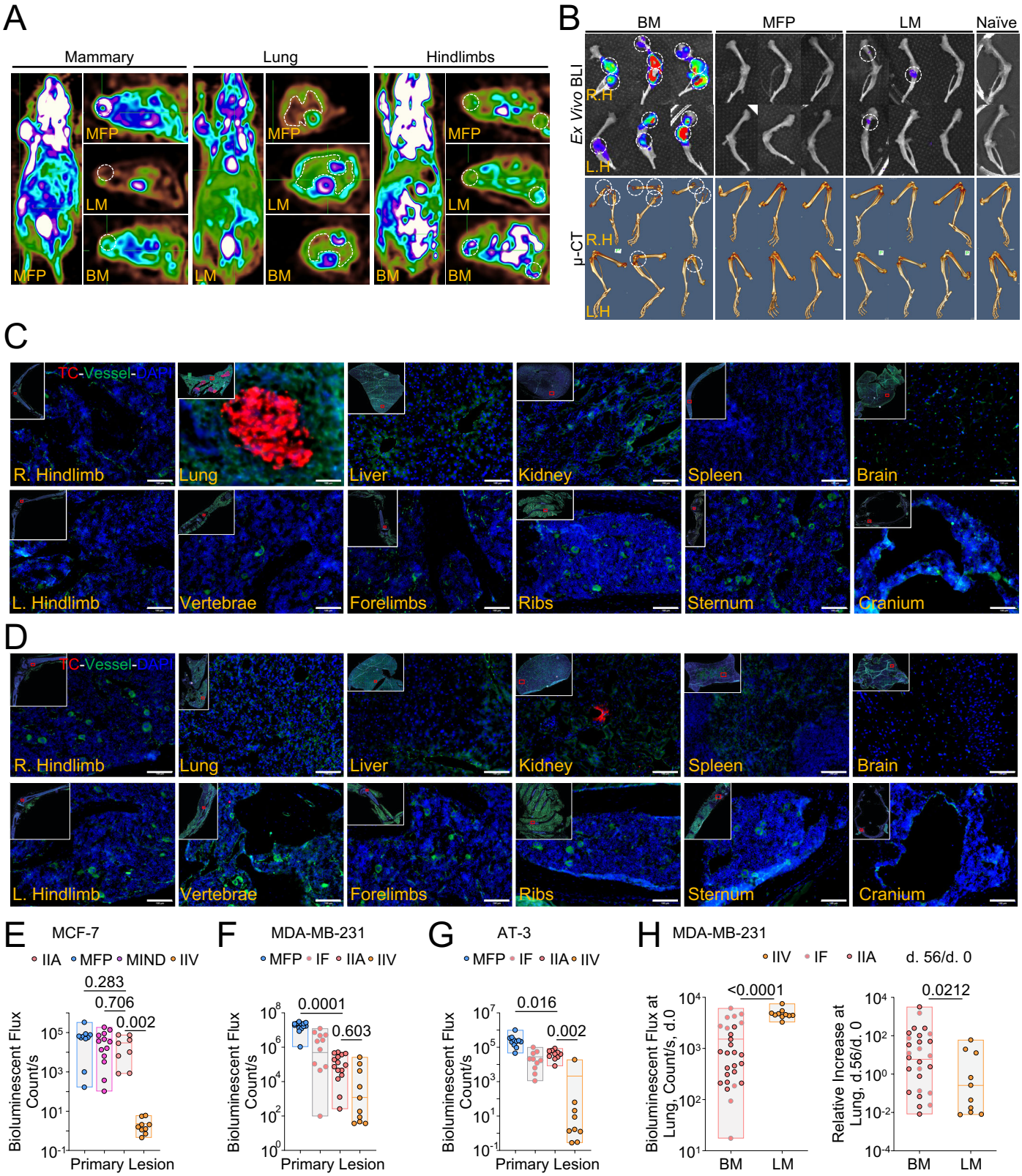
A
Mammary
Lung
Hindlimbs
MFP
LM
BM
B
BM
MFP
LM
Naïve
Ex Vivo BLI
μ-CT
R.H
L.H
C
TC-Vessel-DAPI
R. Hindlimb
Lung
Liver
Kidney
Spleen
Brain
L. Hindlimb
Vertebrae
Forelimbs
Ribs
Sternum
Cranium
D
TC-Vessel-DAPI
R. Hindlimb
Lung
Liver
Kidney
Spleen
Brain
L. Hindlimb
Vertebrae
Forelimbs
Ribs
Sternum
Cranium
E
MCF-7
IIA MFP MIND IIV
0.283
0.706
0.002
Bioluminescent Flux Count/s
Primary Lesion
F
MDA-MB-231
MFP IF IIA IIV
0.0001
0.603
Bioluminescent Flux Count/s
Primary Lesion
G
AT-3
MFP IF IIA IIV
0.016
0.002
Bioluminescent Flux Count/s
Primary Lesion
H
MDA-MB-231
IIV IF IIA
d. 56/d. 0
<0.0001
Bioluminescent Flux at Lung, Count/s, d.0
BM
LM
0.0212
Relative Increase at Lung, d.56/d. 0
BM
LM

Figure S2

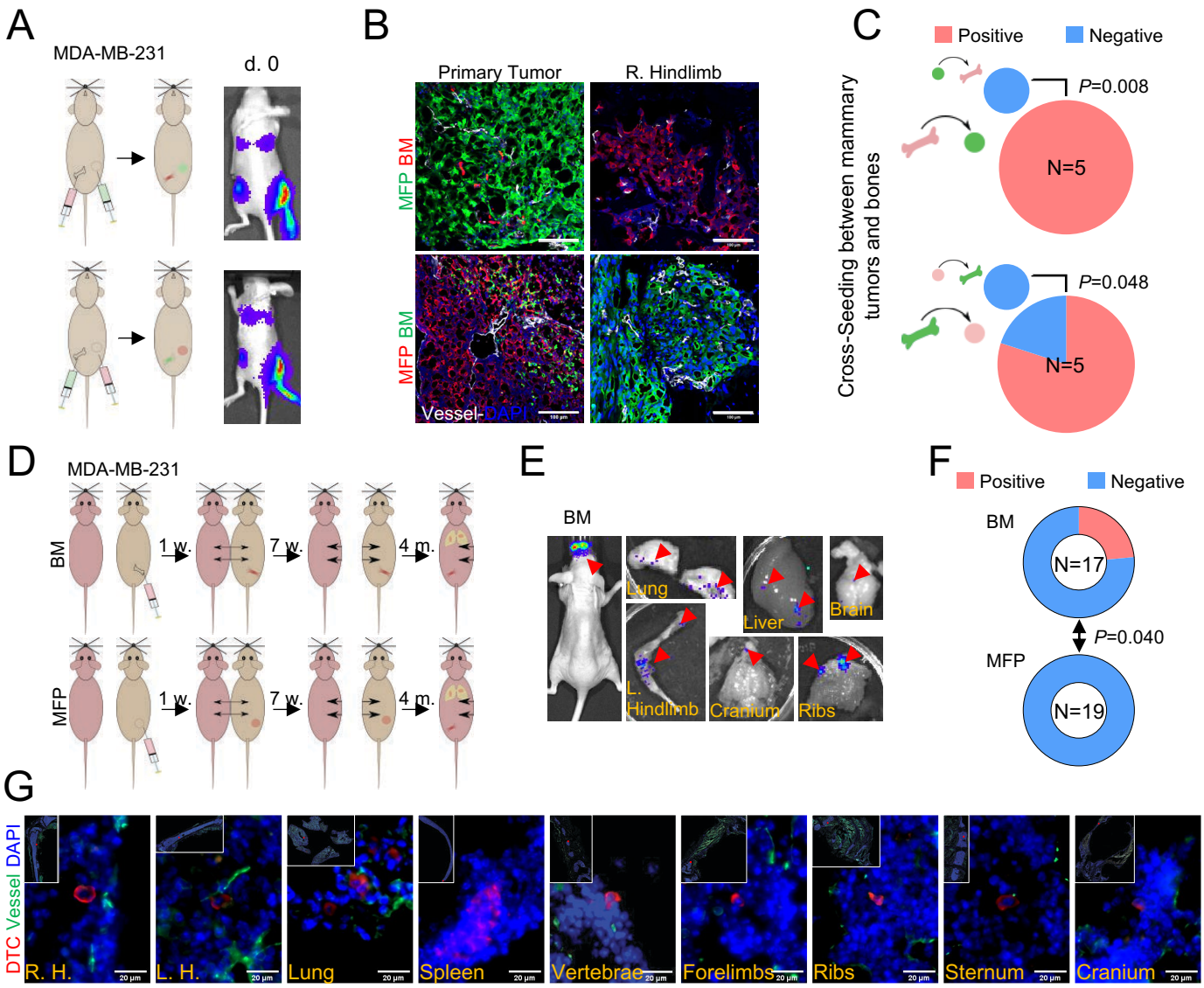
A
MDA-MB-231
d. 0
B
Primary Tumor
R. Hindlimb
MFP BM
MFP BM
Vessel-DAPI
C
Positive
Negative
Cross-Seeding between mammary tumors and bones
P=0.008
N=5
P=0.048
N=5
D
MDA-MB-231
BM
MFP
1 w.
7 w.
4 m.
1 w.
7 w.
4 m.
E
BM
Lung
Liver
Brain
L. Hindlimb
Cranium
Ribs
F
Positive
Negative
BM
N=17
P=0.040
MFP
N=19
G
DTC Vessel DAPI
R. H.
L. H.
Lung
Spleen
Vertebrae
Forelimbs
Ribs
Sternum
Cranium

Figure 3

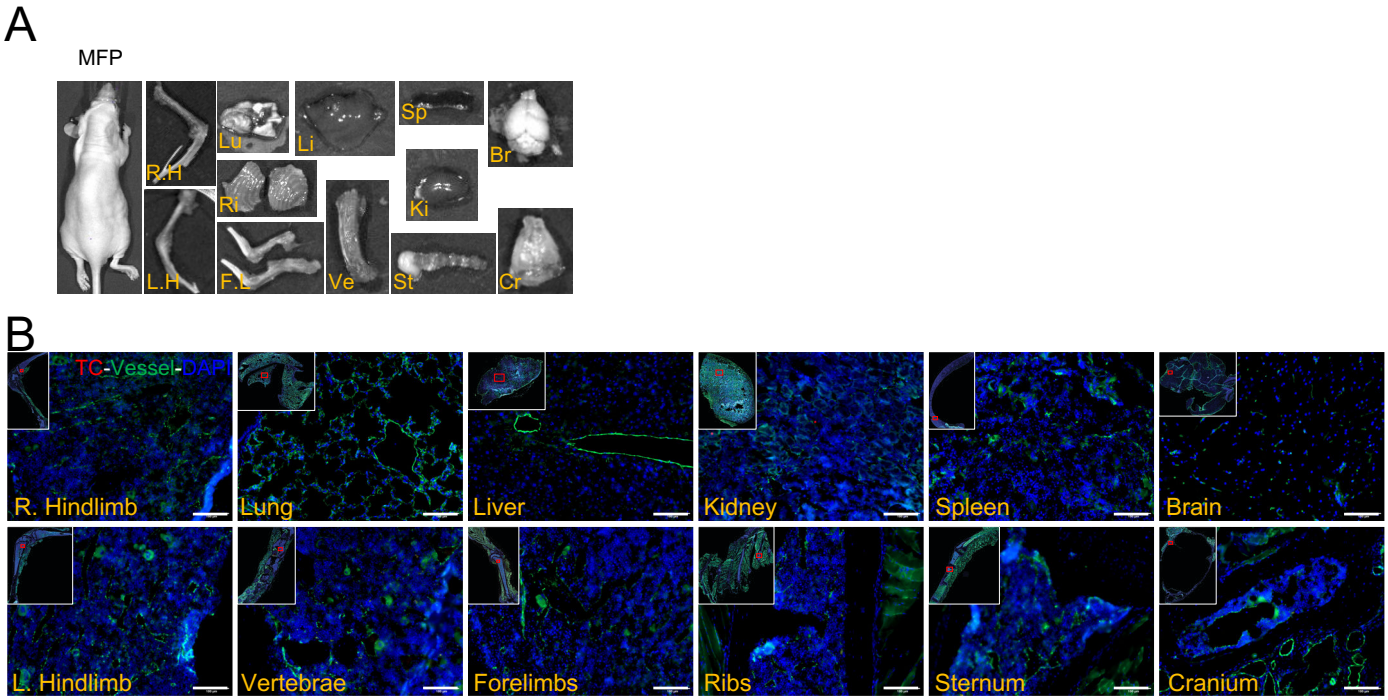
A
MFP
R.H
L.H
Lu
Li
Sp
Br
Ri
Ki
F.L
Ve
St
Cr
B
TC-Vessel-DAPI
R. Hindlimb
Lung
Liver
Kidney
Spleen
Brain
L. Hindlimb
Vertebrae
Forelimbs
Ribs
Sternum
Cranium

Figure S3

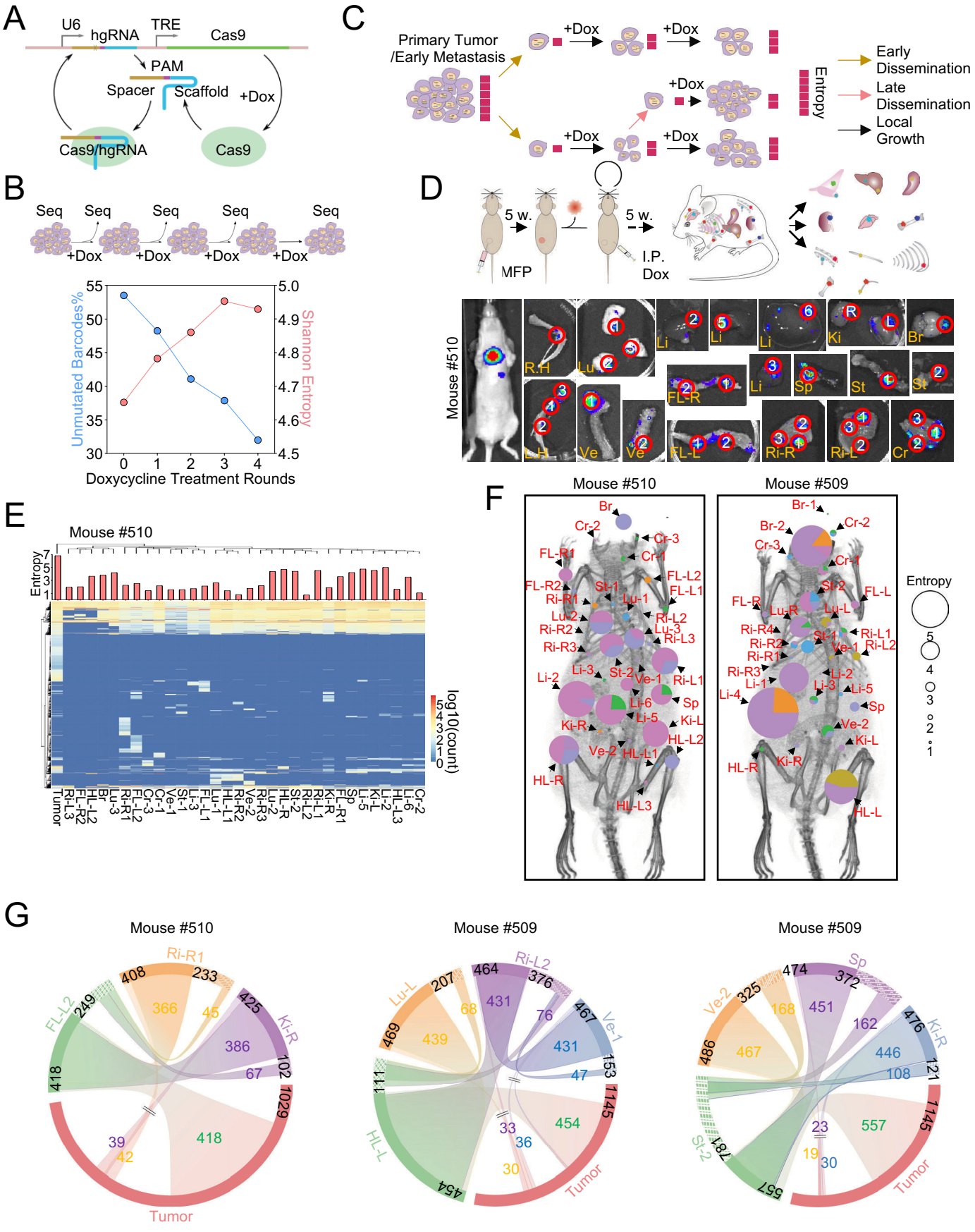
A
U6
hgRNA
TRE
Cas9
PAM
Spacer
Scaffold
+Dox
Cas9/hgRNA
Cas9
B
Seq
+Dox
Unmutated Barcodes%
Shannon Entropy
Doxycycline Treatment Rounds
C
Primary Tumor
/Early Metastasis
+Dox
Entropy
Early Dissemination
Late Dissemination
Local Growth
D
5 w.
MFP
I.P.
Dox
Mouse #510
E
Mouse #510
Entropy
log10(count)
Tumor
F
Mouse #510
Mouse #509
Entropy
G
Mouse #510
Mouse #509
Mouse #509
Tumor

Figure 4

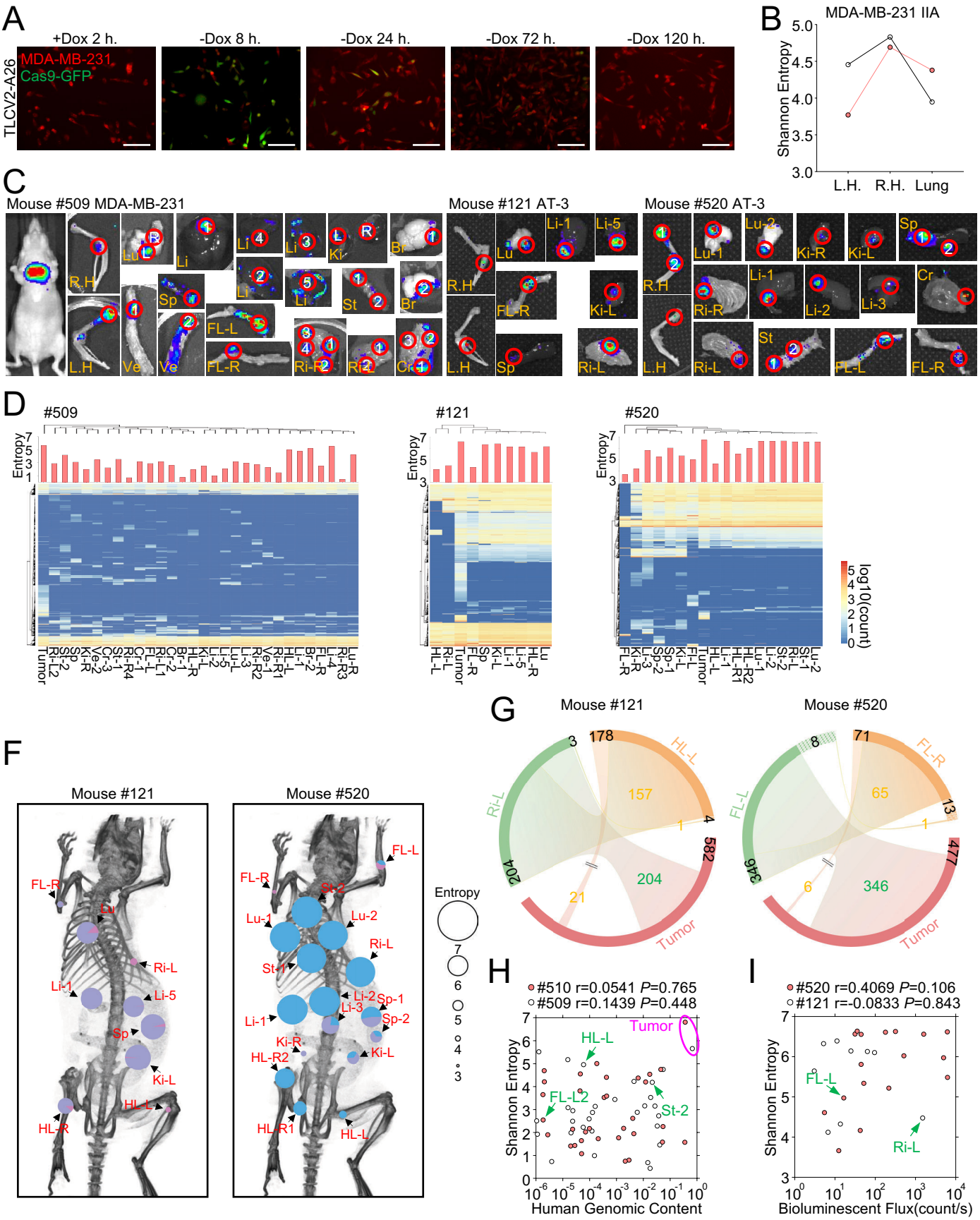
A
+Dox 2 h.
-Dox 8 h.
-Dox 24 h.
-Dox 72 h.
-Dox 120 h.
TLCV2-A26
MDA-MB-231
Cas9-GFP
B
MDA-MB-231 IIA
Shannon Entropy
L.H.
R.H.
Lung
C
Mouse #509 MDA-MB-231
Mouse #121 AT-3
Mouse #520 AT-3
D
#509
#121
#520
Entropy
log10(count)
Tumor
F
Mouse #121
Mouse #520
Entropy
G
Mouse #121
Mouse #520
HL-L
Ri-L
FL-L
FL-R
Tumor
H
#510 r=0.0541 P=0.765
#509 r=0.1439 P=0.448
Shannon Entropy
Human Genomic Content
I
#520 r=0.4069 P=0.106
#121 r=-0.0833 P=0.843
Shannon Entropy
Bioluminescent Flux(count/s)

Figure S4

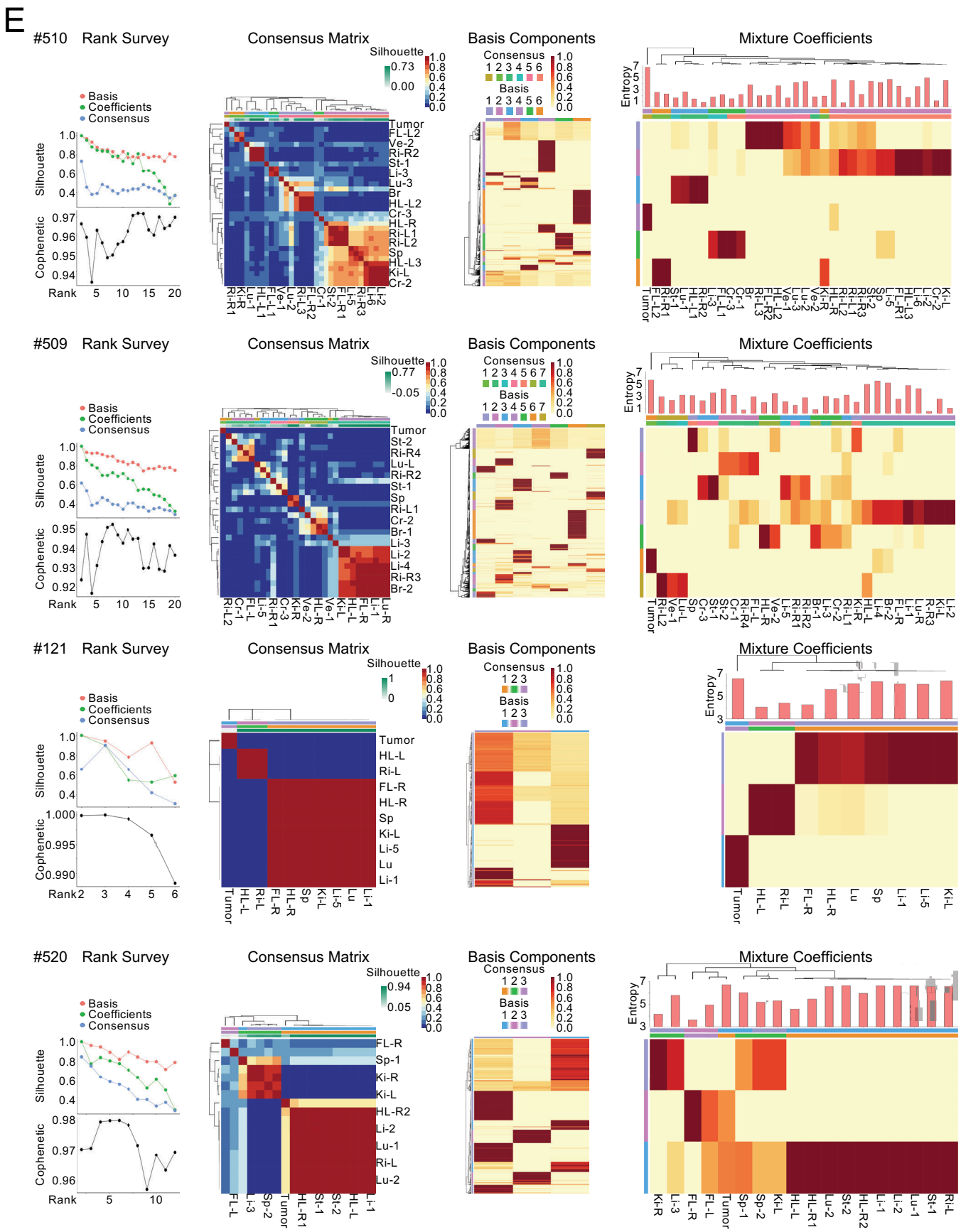
E
#510 Rank Survey
Consensus Matrix
Basis Components
Mixture Coefficients
#509 Rank Survey
Consensus Matrix
Basis Components
Mixture Coefficients
#121 Rank Survey
Consensus Matrix
Basis Components
Mixture Coefficients
#520 Rank Survey
Consensus Matrix
Basis Components
Mixture Coefficients
Basis
Coefficients
Consensus
Silhouette
Cophenetic
Rank
Entropy
Tumor

Figure S4

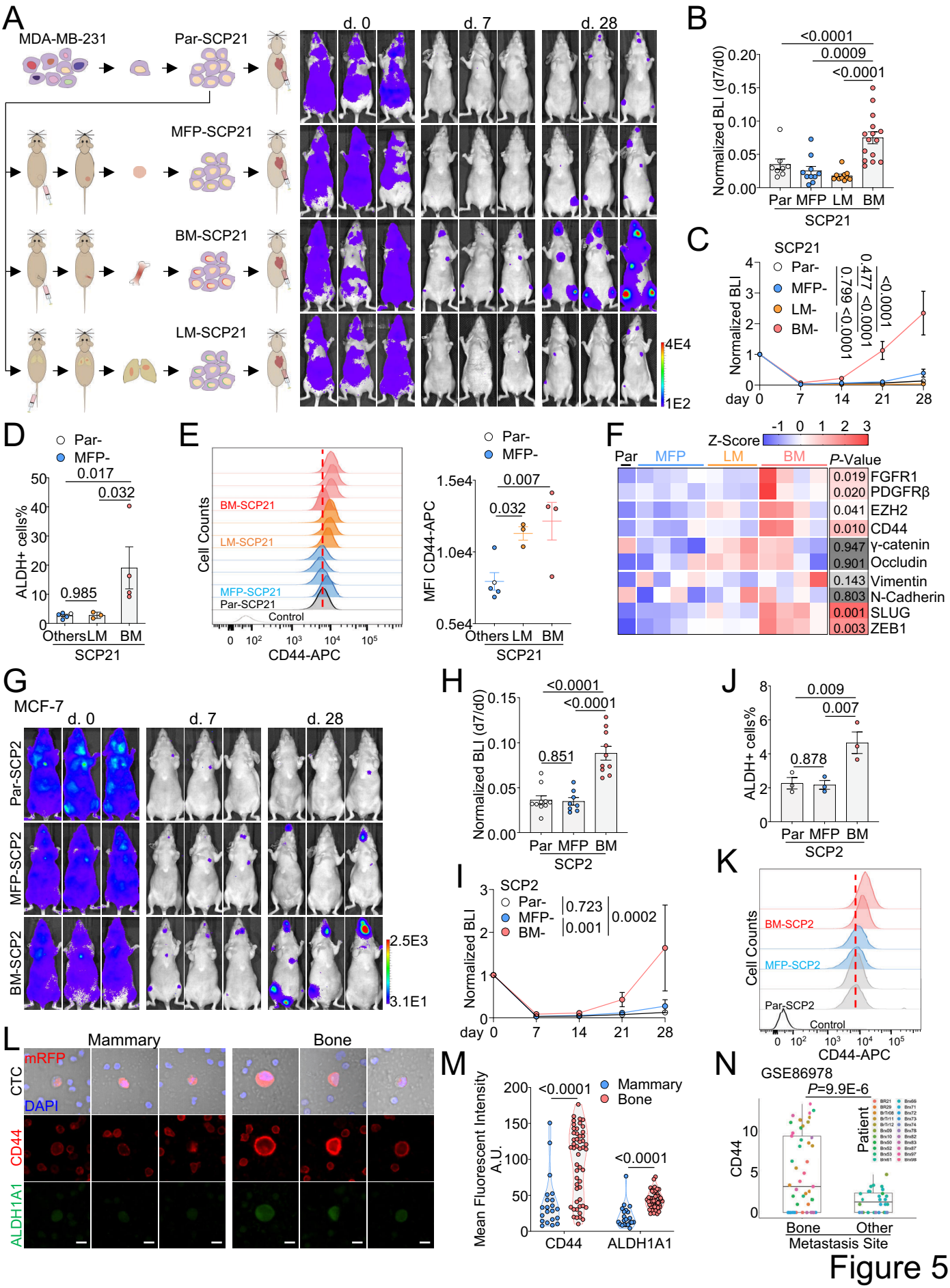
A
MDA-MB-231
Par-SCP21
MFP-SCP21
BM-SCP21
LM-SCP21
d. 0
d. 7
d. 28
4E4
1E2
B
Normalized BLI (d7/d0)
<0.0001
0.0009
<0.0001
Par MFP LM BM
SCP21
C
SCP21
Par-
MFP-
LM-
BM-
Normalized BLI
0.477
<0.0001
0.799
<0.0001
<0.0001
day 0 7 14 21 28
D
Par-
MFP-
ALDH+ cells%
0.017
0.032
0.985
Others LM BM
SCP21
E
Cell Counts
BM-SCP21
LM-SCP21
MFP-SCP21
Par-SCP21
Control
CD44-APC
Par-
MFP-
MFI CD44-APC
0.007
0.032
Others LM BM
SCP21
F
Z-Score
-1 0 1 2 3
Par MFP LM BM
P-Value
0.019 FGFR1
0.020 PDGFRβ
0.041 EZH2
0.010 CD44
0.947 γ-catenin
0.901 Occludin
0.143 Vimentin
0.803 N-Cadherin
0.001 SLUG
0.003 ZEB1
G
MCF-7
d. 0
d. 7
d. 28
Par-SCP2
MFP-SCP2
BM-SCP2
2.5E3
3.1E1
H
Normalized BLI (d7/d0)
<0.0001
<0.0001
0.851
Par MFP BM
SCP2
J
ALDH+ cells%
0.009
0.007
0.878
Par MFP BM
SCP2
I
SCP2
Par-
MFP-
BM-
Normalized BLI
0.723
0.001
0.0002
day 0 7 14 21 28
K
Cell Counts
BM-SCP2
MFP-SCP2
Par-SCP2
Control
CD44-APC
L
Mammary
Bone
CTC
mRFP
DAPI
CD44
ALDH1A1
M
Mean Fluorescent Intensity A.U.
<0.0001
Mammary
Bone
<0.0001
CD44
ALDH1A1
N
GSE86978
P=9.9E-6
CD44
Patient
Bone
Other
Metastasis Site

Figure 5

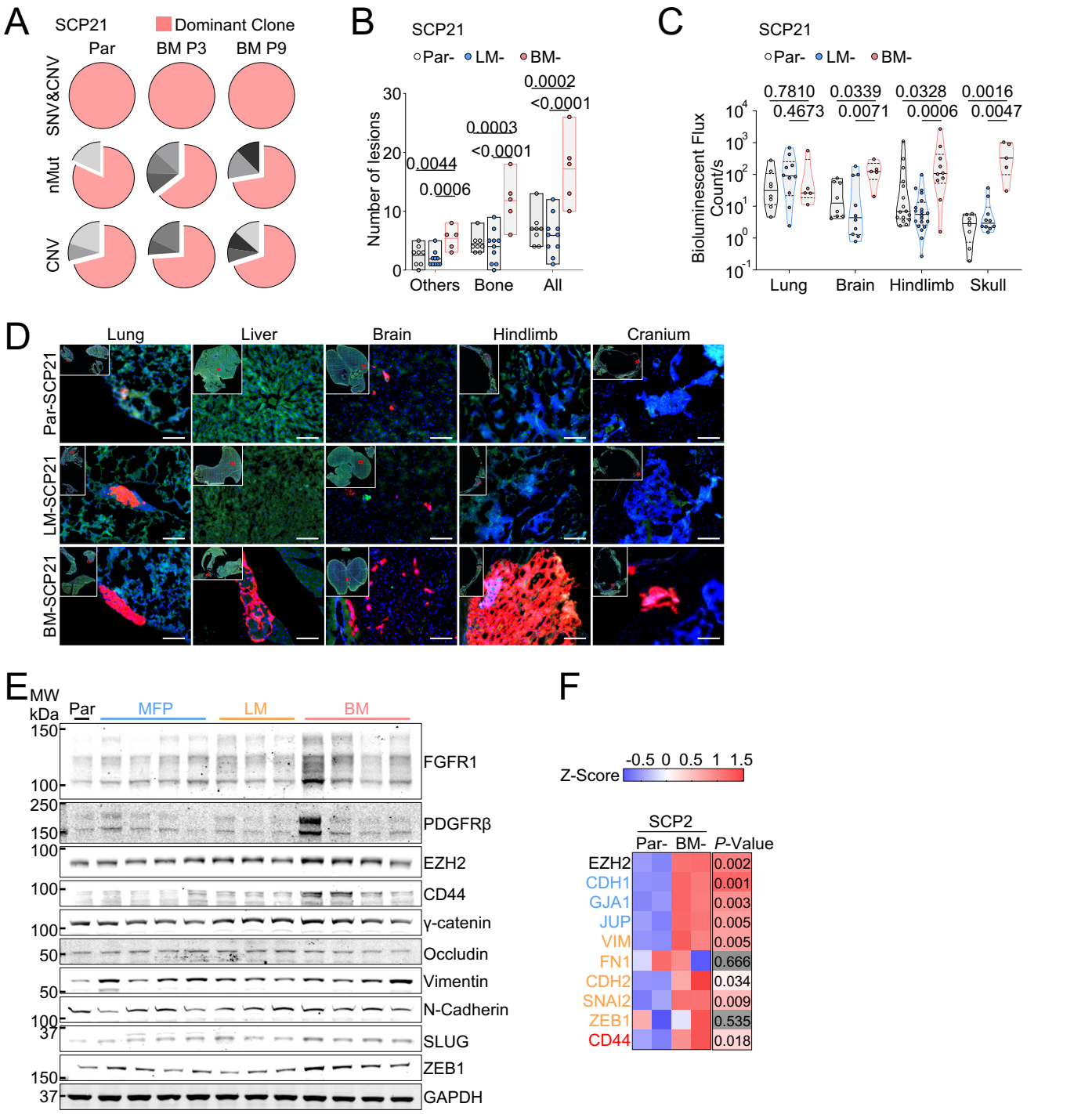
A
SCP21
Dominant Clone
Par
BM P3
BM P9
SNV&CNV
nMut
CNV
B
SCP21
Par- LM- BM-
Number of lesions
0.0044
0.0006
0.0003
<0.0001
0.0002
<0.0001
Others
Bone
All
C
SCP21
Par- LM- BM-
Bioluminescent Flux Count/s
0.7810
0.4673
0.0339
0.0071
0.0328
0.0006
0.0016
0.0047
Lung
Brain
Hindlimb
Skull
D
Lung
Liver
Brain
Hindlimb
Cranium
Par-SCP21
LM-SCP21
BM-SCP21
E
MW kDa
Par
MFP
LM
BM
FGFR1
PDGFRβ
EZH2
CD44
γ-catenin
Occludin
Vimentin
N-Cadherin
SLUG
ZEB1
GAPDH
F
Z-Score
-0.5 0 0.5 1 1.5
SCP2
Par- BM-
P-Value
EZH2 0.002
CDH1 0.001
GJA1 0.003
JUP 0.005
VIM 0.005
FN1 0.666
CDH2 0.034
SNAI2 0.009
ZEB1 0.535
CD44 0.018

Figure S5

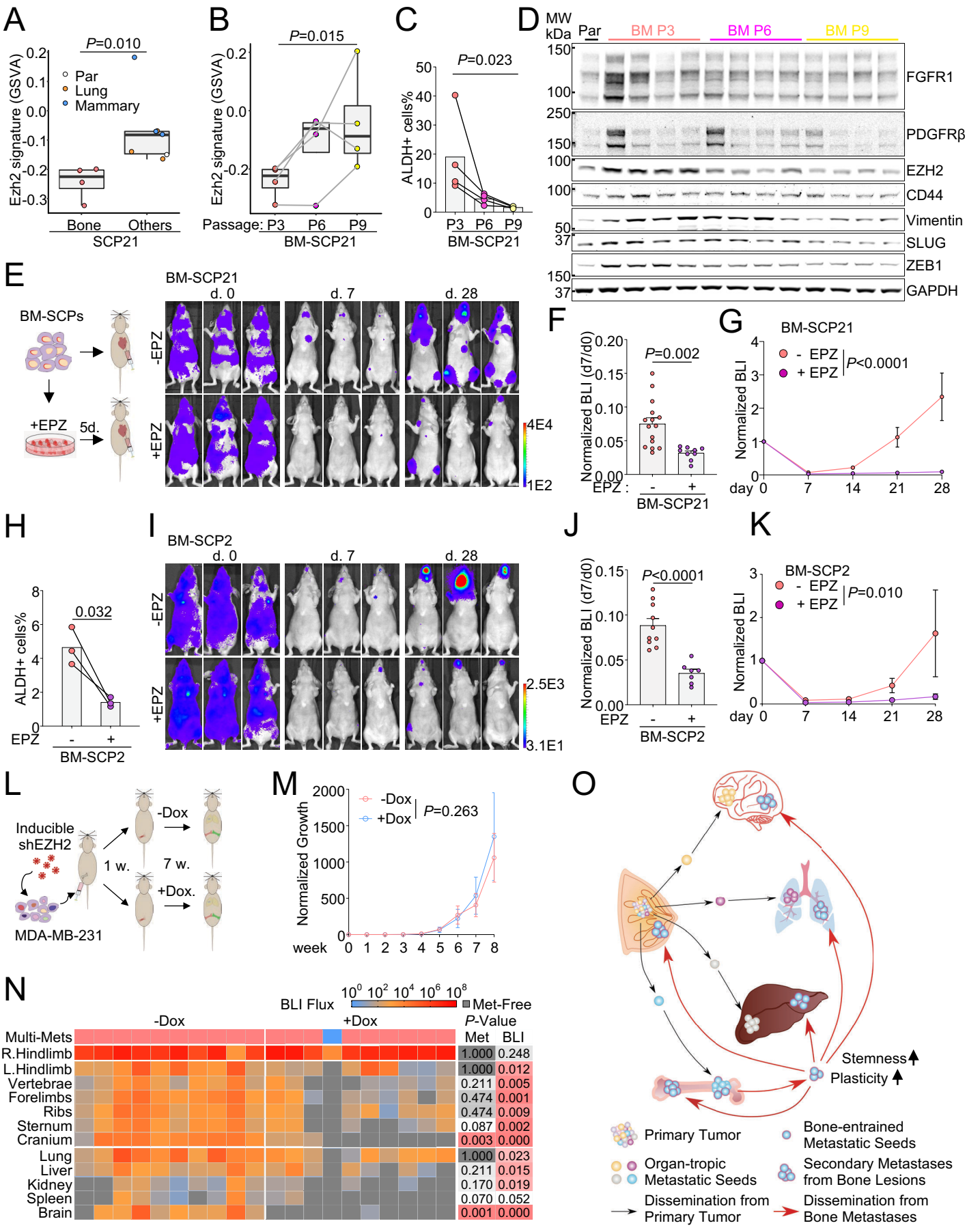
A
P=0.010
Par
Lung
Mammary
Ezh2 signature (GSVA)
Bone
Others
SCP21
B
P=0.015
Ezh2 signature (GSVA)
Passage: P3 P6 P9
BM-SCP21
C
P=0.023
ALDH+ cells%
P3 P6 P9
BM-SCP21
D
MW kDa
Par
BM P3
BM P6
BM P9
FGFR1
PDGFRβ
EZH2
CD44
Vimentin
SLUG
ZEB1
GAPDH
E
BM-SCP21
d. 0
d. 7
d. 28
BM-SCPs
+EPZ
5d.
-EPZ
+EPZ
4E4
1E2
F
P=0.002
Normalized BLI (d7/d0)
EPZ :
BM-SCP21
G
BM-SCP21
- EPZ
+ EPZ
P<0.0001
Normalized BLI
day 0 7 14 21 28
H
0.032
ALDH+ cells%
EPZ
BM-SCP2
I
BM-SCP2
d. 0
d. 7
d. 28
-EPZ
+EPZ
2.5E3
3.1E1
J
P<0.0001
Normalized BLI (d7/d0)
EPZ
BM-SCP2
K
BM-SCP2
- EPZ
+ EPZ
P=0.010
Normalized BLI
day 0 7 14 21 28
L
Inducible shEZH2
MDA-MB-231
1 w.
-Dox
7 w.
+Dox.
M
-Dox
+Dox
P=0.263
Normalized Growth
week 0 1 2 3 4 5 6 7 8
N
BLI Flux
Met-Free
-Dox
+Dox
P-Value
Met BLI
Multi-Mets
R.Hindlimb 1.000 0.248
L.Hindlimb 1.000 0.012
Vertebrae 0.211 0.005
Forelimbs 0.474 0.001
Ribs 0.474 0.009
Sternum 0.087 0.002
Cranium 0.003 0.000
Lung 1.000 0.023
Liver 0.211 0.015
Kidney 0.170 0.019
Spleen 0.070 0.052
Brain 0.001 0.000
O
Stemness
Plasticity
Primary Tumor
Bone-entrained Metastatic Seeds
Organ-tropic Metastatic Seeds
Secondary Metastases from Bone Lesions
Dissemination from Primary Tumor
Dissemination from Bone Metastases

Figure 6

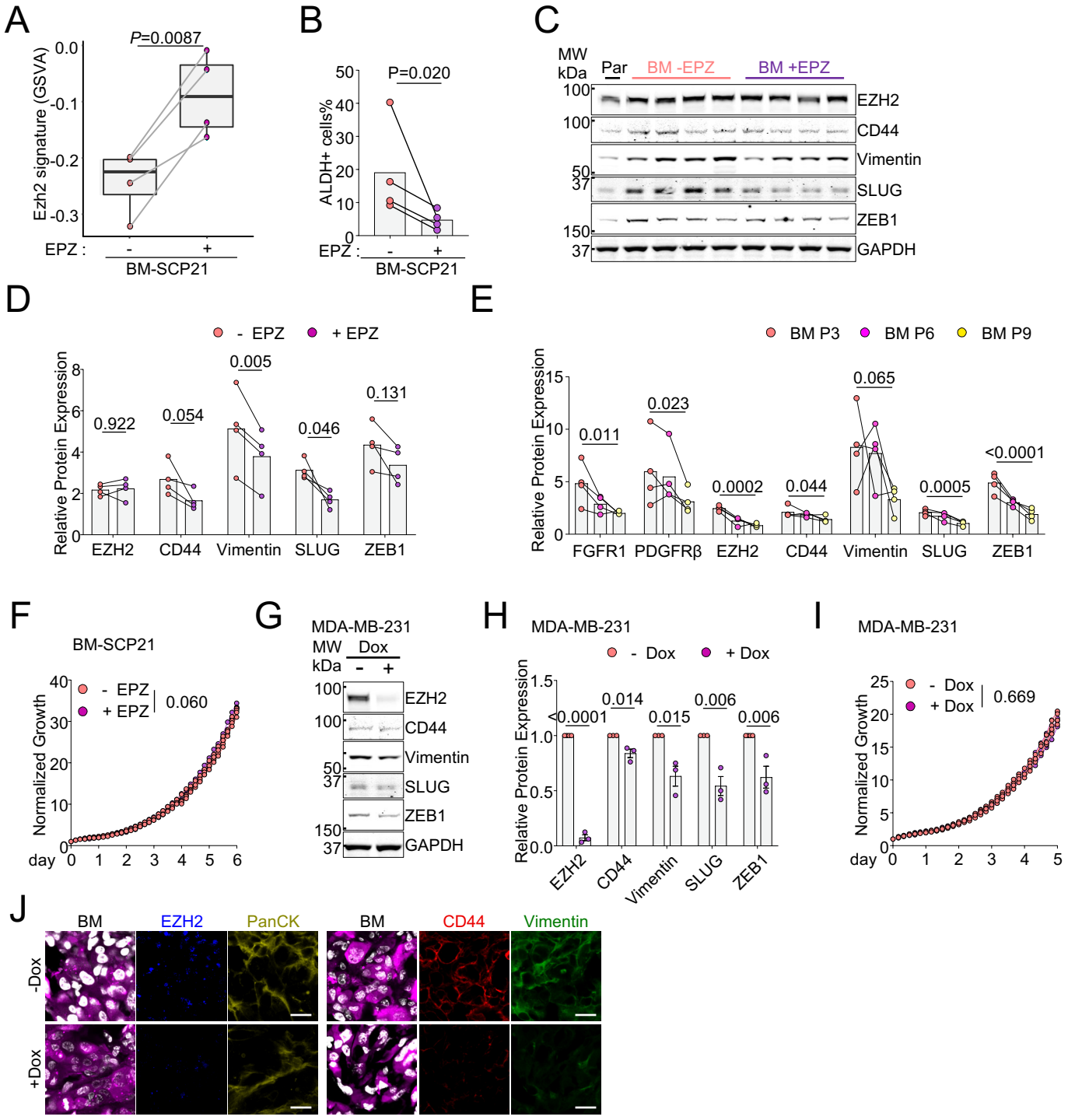
A
P=0.0087
Ezh2 signature (GSVA)
EPZ :
BM-SCP21
B
P=0.020
ALDH+ cells%
EPZ :
BM-SCP21
C
MW kDa
Par
BM -EPZ
BM +EPZ
EZH2
CD44
Vimentin
SLUG
ZEB1
GAPDH
D
- EPZ
+ EPZ
Relative Protein Expression
0.922
0.054
0.005
0.046
0.131
EZH2
CD44
Vimentin
SLUG
ZEB1
E
BM P3
BM P6
BM P9
Relative Protein Expression
0.011
0.023
0.0002
0.044
0.065
0.0005
<0.0001
FGFR1
PDGFRβ
EZH2
CD44
Vimentin
SLUG
ZEB1
F
BM-SCP21
- EPZ
+ EPZ
0.060
Normalized Growth
day
G
MDA-MB-231
MW kDa
Dox
EZH2
CD44
Vimentin
SLUG
ZEB1
GAPDH
H
MDA-MB-231
- Dox
+ Dox
Relative Protein Expression
<0.0001
0.014
0.015
0.006
0.006
EZH2
CD44
Vimentin
SLUG
ZEB1
I
MDA-MB-231
- Dox
+ Dox
0.669
Normalized Growth
day
J
BM
EZH2
PanCK
BM
CD44
Vimentin
-Dox
+Dox

Figure S6